

Non-linear bending analysis of shear deformable functionally graded rotating disk



M. Kadkhodayan^{a,*}, M.E. Golmakani^b

^a Department of Mechanical Engineering, Ferdowsi University of Mashhad, Mashhad, Iran

^b Department of Mechanical Engineering, Mashhad Branch, Islamic Azad University, Mashhad, Iran

ARTICLE INFO

Article history:

Received 4 December 2010

Received in revised form

22 June 2013

Accepted 23 August 2013

Available online 4 September 2013

Keywords:

Functionally graded rotating disk

Non-linear bending

DR method

ABSTRACT

This study investigates the non-linear analysis of functionally graded solid and hollow rotating axisymmetric disks with uniform and variable thicknesses subjected to bending load. The material properties of the constituent components of the FG disk are assumed to be represented by the Mori–Tanaka distribution along the radial direction. The non-linear formulations are based on first-order shear deformation theory (FSDT) and the large deflection von-Karman equations. The dynamic relaxation (DR) method combined with the finite difference discretization technique is employed to solve the equilibrium equations. The effects of the grading index, angular velocity, geometry, thickness-to-radius ratio and thickness profile of the disk are studied in detail.

© 2013 Elsevier Ltd. All rights reserved.

1. Introduction

Because of the importance of rotating disks in engineering applications such as in steam and gas turbines, flywheel systems, brake disks and clutches, researches on the behavior of these basic structures have been never stopped. In the all mentioned samples, body forces and bending loads are applied to a hollow or solid rotating disk. For example, the pressure difference across the rotors, as well as rotational stresses, causes bending in gas turbine rotors. Moreover, the force responsible for maintaining contact between the rotating disks leads to the bending in clutches [1]. These samples highlight the role of bending load in the design and analysis of rotating components. In all these applications, the performance of the components considering efficiency and service life depends on the material properties, geometry, boundary conditions and applied loads. Generally, these components can be manufactured using any metal. However, for some specific applications, they are fabricated using special materials. In the latter half of 20th century, composite materials have gained wide usage in engineering applications because of their benefits, including high strength. These structures have some disadvantages because of the different physical and mechanical properties of the two different layers and the discontinuity at the interface [2]. A new group of materials called functionally graded materials (FGMs) was introduced in 1984 by a group of material scientists in Japan to overcome these disadvantages [3]. FGMs made of ceramic and metal are capable of both suffering from high-temperature environment because of better thermal resistance of the ceramic phase [4] and being

toughened by the metallic composition. Because of the advantages of FGMs over conventional composites and monolithic materials, these materials have been extensively studied for potential applications as structural elements, such as FGM beams, plates, shells, and cylinders [5]. FGMs belong to a new class of materials which are microscopically heterogeneous and their material properties vary continuously [6]. The material properties of FGMs show a continuous and smooth change from one surface to another by gradually changing the volume fraction of the constituent materials. Many studies on linear thermal bending of FGM plates are available in the literature. However, investigations in non-linear analysis of FGM plates under thermal or mechanical loadings are limited in number [7]. Because of the increasing use of FGMs, it is important to understand the non-linear behavior of functionally graded rotating disks under transverse loads. Many studies on the linear and thermoelastic behavior of rotating FG disks without consideration of transverse loads have been performed based on different plate theories. Durodola and Attia [8] conducted a finite element analysis for FG rotating disks using commercial software. Afsar and Go [5] carried out the finite element analysis of different thermoelastic fields in a thin circular FG rotating disk. Several works presented semi-analytical and thermoelastic solutions for hollow and solid rotating axisymmetric disks made of functionally graded materials under plane stress conditions [9–12]. In their works, a set of linear algebraic equations were obtained by dividing the radial domain into some virtual sub-domains. Ghafoori [13] expressed the shortcomings of study done by Hosseini Kordkheili and Naghdabadi [9]. They obtained the Navier thermoelastic equation and applied several incorrect coefficients, which resulted in considerable errors in their numerical results. In all the studies mentioned, the effect of the transverse load on the linear behavior of rotating disks was not considered. Recently, a few studies were conducted on the small deflection of FG rotating disks with transverse loads by Bayat et al.

* Corresponding author. Tel.: +98 9153 111869.

E-mail addresses: kadkhoda@um.ac.ir (M. Kadkhodayan), m.e.golmakani@mshdiau.ac.ir (M.E. Golmakani).

[14,15]. In their works, a semi-analytical solution was given for the bending analysis of FG rotating disks under different types of boundary conditions applied to solid and hollow disks with uniform and variable thicknesses based on first-order shear deformation theory (FSDT). Moreover, Bayat et al. [16] used new linear and non-linear equilibrium equations for FG axisymmetric rotating disk with bending and thermal loadings based on FSDT and von-Karman theories. In their study, the material properties of FGM disks were assumed to vary continuously through the thickness according to a power-law distribution of the volume fraction of the constituents. Sahraee [17] studied the effect of transverse shear strains through the thickness using classical and shear deformation plate theories. The simplest shear deformation plate theory, FSDT, can be classified, depending on whether or not the expansion of displacement components or stress components through the thickness of plate is assumed to be known a priori [17]. In order to consider the effect of shear deformations, analyzing a plate statically Reissner [18] developed a stress-based theory while Mindlin [19] by analyzing a plate dynamically developed a displacement-based theory which include the effects of transverse shear deformations and rotary inertia (for more details see [20–25]). Reddy et al. [23] considered axisymmetric bending and stretching of FG solid and annular circular plates using FSDT. Yang and Shen [24] studied non-linear bending analysis of shear deformable FGM rectangular plates subjected to transverse and in-plane loads under various boundary conditions and by the aid of a semi-analytical-numerical method. Using Reissner and von-Karman plate equations, Reddy and Huang [25] studied non-linear axisymmetric bending of variable thickness orthotropic annular plates. Variable thickness plates (or disks) have always been attractive for designers, and a lot of researches have been carried out on this subject [26]. The investigation of disks with varying thickness is important in applied engineering because such geometries can improve the material potential by decreasing the self-weight and enhancing the distribution of stress and displacement [1,12,27]. When the thickness along the radius of a disk varies, finding a closed-form solution becomes very difficult [27]. To the best of our knowledge, no study has used a non-linear analysis of FG disks with uniform and variable thickness subjected to a transverse load and an inertia force due to rotation. To be more specific, in this paper, a thin FG disk of variable thickness subjected to inertia and bending transverse loads under various boundary conditions is investigated. The material properties of the constituent components of the FG disk are assumed to be represented by the Mori-Tanaka distribution [28], a micromechanics-based method for determining effective material properties of the FGM, along the radial direction. Moreover, some studies are conducted by the simple rule of mixtures for comparison between these two schemes. The constitutive equations are obtained based on FSDT using the von-Karman theory for large deflections. The dynamic relaxation (DR) method along with the finite difference discretization technique is employed to solve the disk field equations. Numerical results are presented graphically to show how the grading index parameter, angular velocity, boundary conditions and thickness profile of the disk affect different parameters such as the resultant stresses and displacements.

2. Problem formulation

2.1. FGM material properties

There are some models to express the variation of material properties in FGMs in the literature. The functions are continuous, simple and able to represent realistic properties of actual FGMs. The most commonly used model is the power-law distribution of the volume fraction. However, the elastic properties of actual FGMs are very different than those estimated by simple rules of mixture.

The prediction of the macroscopic stress-strain response of composite materials depends on the description of their complex microstructural behaviors represented by the interaction between the constituents. Therefore, using a micromechanics-based method for FGM's material properties such as Mori-Tanaka theory can represent the realistic prediction for the behavior of the FG disk. These schemes provide efficient and straight forward algorithms for the prediction of the elastic constants. These methods are based on two steps to predict the macroscopic response. In the first step, a local problem for a single inclusion is solved to obtain an approximate local field behavior and in the second step the global fields are obtained by averaging the local ones [29]. In the current study, the Mori-Tanaka scheme [28–30] was used for the modeling of elastic properties. Furthermore, to compare the results obtained by this theory and the simple rules of mixture, several studies were conducted using a power-law distribution. According to the simple rule of mixture, the material properties along the radius of the disk P can be expressed as

$$P(r) = (P_c - P_m)V_c + P_m, \quad (1)$$

where $P(r)$ denotes a generic material property and the P_m and P_c denote the properties of the metallic and ceramic constituents, respectively. The inner and outer surfaces of the FG disk, r_i and r_o , are assumed to be metal-rich and ceramic-rich, respectively. The volume fractions of the metal V_m and ceramic V_c corresponding to the power law are assumed to be

$$\begin{cases} V_c = \left(\frac{r-r_i}{r_o-r_i}\right)^n, \\ V_m = 1 - V_c, \end{cases} \quad (2)$$

where r is the radial coordinate ($r_i \leq r \leq r_o$) and n is a grading index that dictates the material variation profile. Accordingly, the assumed form for the modulus of elasticity E and mass density ρ is the following:

$$E(r) = (E_c - E_m) \left(\frac{r-r_i}{r_o-r_i}\right)^n + E_m, \quad (3)$$

$$\rho(r) = (\rho_c - \rho_m) \left(\frac{r-r_i}{r_o-r_i}\right)^n + \rho_m. \quad (4)$$

For many engineering materials, Poisson's ratio is within the range of 0.25–0.35 and varies slightly. Therefore, for simplicity, Poisson's ratio is assumed to be a constant in the following study. However, the variable Poisson's ratio along the radial direction does not give rise to any difficulty in determining the solution [31]. The effective bulk modulus, K , and the effective shear modulus, G , of the functionally gradient material based on the Mori-Tanaka homogenization method [30] are the following:

$$\begin{cases} \frac{K-K_c}{K_m-K_c} = \frac{V_m}{1 + (1-V_m)\frac{K_m-K_c}{K_c + (4/3)G_c}}, \\ \frac{G-G_c}{G_m-G_c} = \frac{V_m}{1 + (1-V_m)\frac{G_m-G_c}{G_c + f_c}}, \end{cases} \quad (5)$$

where

$$f_c = \frac{G_c(9K_c + 8G_c)}{6(K_c + 2G_c)}. \quad (6)$$

Based on this method, the effective values of Young's modulus E are computed using:

$$E = \frac{9KG}{3K + G}. \quad (7)$$

2.2. Governing equations

In this section, the fundamental equations of the large deflection analysis of pressure-loaded FG rotating disks are briefly outlined. Consider a thin, axisymmetric FG disk with variable thickness, inner radius r_i and outer radius r_o at a constant angular velocity ω about the

central axis perpendicular to the plane of the disk under different boundary conditions, as shown in Fig. 1. An axisymmetric transverse loading $q_z(r) = q$ is applied to the disk. Due to the axial symmetry in geometry and loading, cylindrical coordinates (r, θ, z) are used. The first-order shear deformation plate theory (FSDT) is applied in this work [32]. In FSDT, the transverse shear strain is assumed to be constant with respect to the thickness coordinate. Thus

$$\begin{cases} u_r(r, z) = u_0(r) + z\psi(r), \\ u_z(r, z) = w(r), \end{cases} \quad (8)$$

where u_r and u_z are the components of radial and vertical displacement at a general point, respectively, while u_0 and w are similar components at the middle surfaces ($z=0$). The parameter ψ is rotation of the middle surface (i.e., $z=0$) of the plate in the θ direction. Using Eq. (8) and the non-linear von-Karman strain-displacement relations gives the following expressions:

$$\begin{cases} \epsilon_r = \frac{du_0}{dr} + \frac{1}{2} \left(\frac{d\psi}{dr} \right)^2 + z \frac{dw}{dr}, \\ \epsilon_\theta = \frac{u_0}{r} + z \frac{\psi}{r}, \\ \gamma_{rz} = \psi + \frac{dw}{dr}, \end{cases} \quad (9)$$

where ϵ_r and ϵ_θ are the normal strains along the r and θ directions and γ_{rz} is the shear strain. According to Hooke's law for a plate, the stress-strain relationships for the FGMs are given by the following equation:

$$\begin{cases} \sigma_r = \frac{E}{(1-\nu^2)} [\epsilon_r + \nu\epsilon_\theta], \\ \sigma_\theta = \frac{E}{(1-\nu^2)} [\epsilon_\theta + \nu\epsilon_r], \\ \sigma_{rz} = \frac{E}{2(1+\nu)} \gamma_{rz}, \end{cases} \quad (10)$$

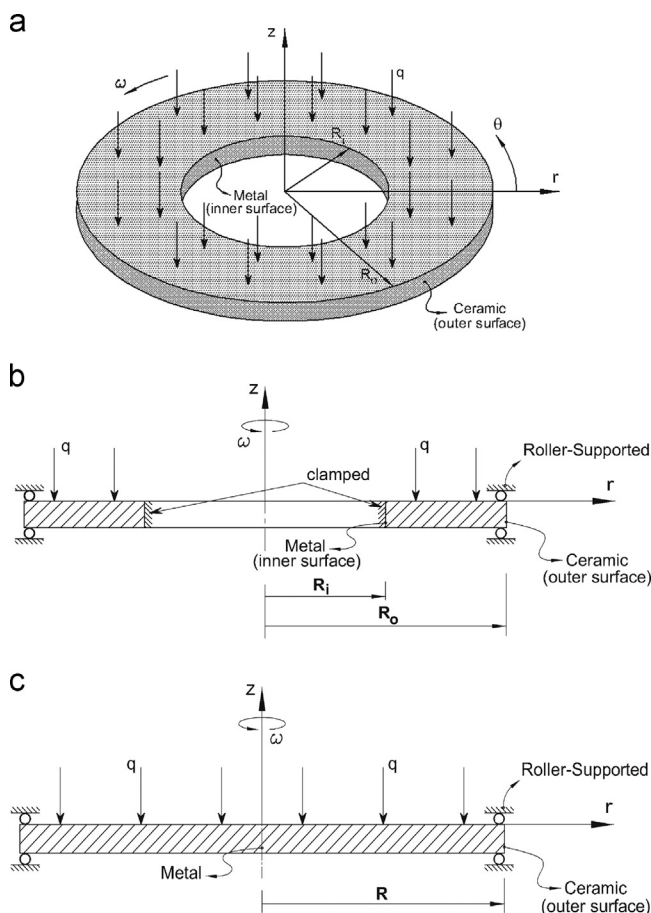


Fig. 1. A rotating functionally graded clamped-roller supported hollow (a, b) and roller supported solid (c) disk subjected to a uniform transverse load.

where $E = E(r)$. As aforementioned, variable thickness disks are widely used in many kinds of engineering applications, and further study of their behaviors is required. The thickness profile h of the plate is assumed to vary with radius according to the following equation

$$h(r) = h_0 \left(1 - S \left(\frac{r}{r_0} \right)^{m_1} \right) \quad (11)$$

where S and m_1 are geometric parameters such that $0 \leq S < 1$, $m_1 > 0$ and h_0 is the thickness at the center of the plate. A uniform thickness disk can be obtained from Eq. (11) by setting $S = 0$, whereas a linearly decreasing thickness can be obtained for $S \neq 0$ and $m_1 = 1$. The profile is concave if $m_1 < 1$, and it is convex if $m_1 > 1$ (see [12,15]). Hence, according to [1,12,15] the values of S are taken as 0.96, 0.5 and 0.415 for concave, linear and convex profiles, respectively. Moreover, the values of m_1 for the mentioned profiles are 0.5, 1.0 and 3.0, respectively. Different forms of the thickness profiles for various S and m_1 are shown in Fig. 2. To compare the effect of thickness variation on the results, all the thickness profiles should possess the same volume. The condition to achieve the same volume of disk depends upon the value of thickness that can be adjusted accordingly. The values of S and m_1 in this study have been chosen so that each thickness profile has almost 80% thickness reduction at the edge of the disk [12,15,33]. The weight values of FG disk for different types of thickness profiles and

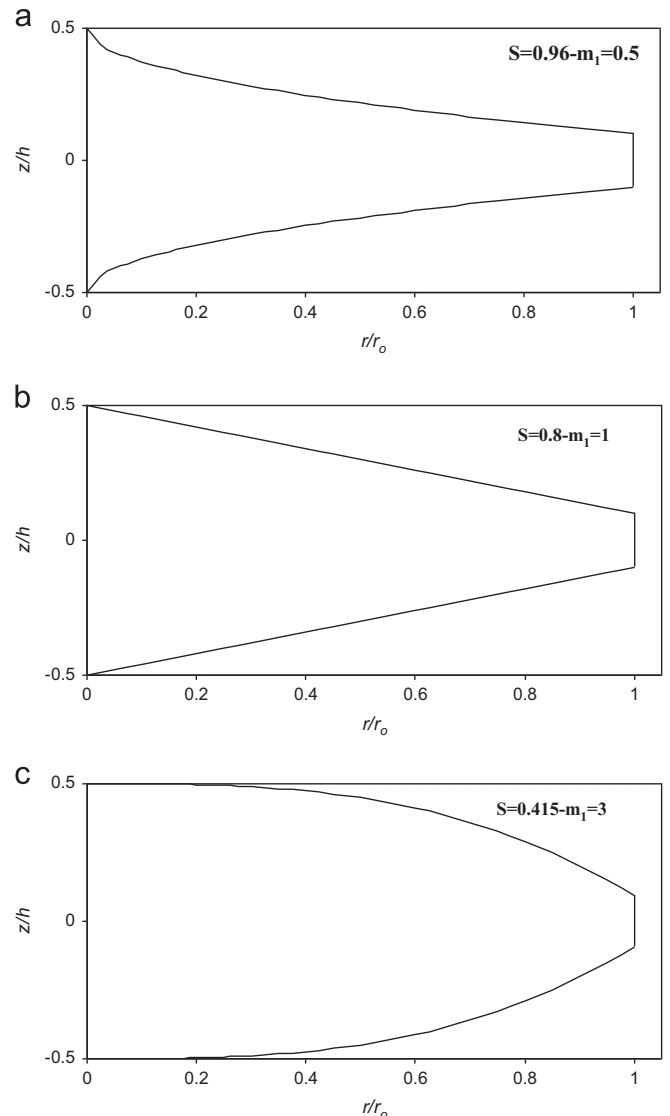


Fig. 2. Thickness profile of FG solid disks: (a) concave, (b) linear and (c) convex.

Table 1
Effect of grading index n and thickness profile on the weight ratio W/W_c (see Ref. [12]).

Thickness profile	Full-ceramic ($n=0$)	$n=0.2$	$n=1.5$	$n=5.0$	Full-metal ($n \rightarrow \infty$)
Concave: $S=0.96$ and $m_1=0.5$	1.0	0.9054	0.6538	0.5312	0.4737
Linear: $S=0.8$ and $m_1=1.0$	1.0	0.9178	0.6864	0.5552	0.4737
Convex: $S=0.415$ and $m_1=3.0$	1.0	0.9317	0.7219	0.5820	0.4737
Uniform: $S=0.0$	1.0	0.9389	0.7444	0.6032	0.4737

grading indices n are inserted in Table 1. To compute the weight ratio of FG disk to ceramic one, W/W_c , the following relation is used [12]:

$$\frac{W}{W_c} = \frac{\int_{r_i}^{r_o} r \left((\rho_o - \rho_i) \left(\frac{r-r_i}{r_o-r_i} \right)^n + \rho_i \right) \left(1 - S \left(\frac{r}{r_o} \right)^{m_1} \right) dr}{\int_{r_i}^{r_o} r \rho_o \left(1 - S \left(\frac{r}{r_o} \right)^{m_1} \right) dr} \quad (12)$$

The effect of thickness profile can be revealed by comparing the weight values for the same value of grading index, n . It is seen that the hollow FG wheel with the concave thickness profile has smaller weight compared to that of other thickness profiles [12]. To show the effect of grading index n on the weight, wheel with the same thickness profile is also investigated. It is noticed that the weights of FG wheels are placed between $\rho_m/\rho_c = 2700/5700 = 0.4737$ and 1. Moreover, it is observed from Table 1 that for different values of grading indices n the weight ratio of the FG disk to ceramic one, W/W_c , is approximately constant for different thickness profiles. Hence, the selected values of S and m_1 for modeling different types of thickness profiles are approved. Using the principle of virtual displacements, the following equilibrium equations can be derived:

$$\begin{cases} \frac{dN_r}{dr} + \frac{1}{r}(N_r - N_\theta) + \rho_1 r \omega^2 = 0, \\ \frac{dM_r}{dr} + \frac{1}{r}(M_r - M_\theta) - Q_r = 0, \\ \frac{dQ_r}{dr} + \frac{Q_r}{r} + N_r \frac{d^2 w}{dr^2} + (N_\theta - \rho_1 r \omega^2) \frac{dw}{dr} + q = 0. \end{cases} \quad (13)$$

The variables ($N_r, N_\theta, M_r, M_\theta, Q_r$) and the mean of the density along the thickness (ρ_1) in (13) can be obtained by using appropriate integration through the thickness:

$$\begin{cases} (N_r, N_\theta, Q_r) = \int_{-h(r)/2}^{h(r)/2} (\sigma_r, \sigma_\theta, \sigma_{rz}) dz, \\ (M_r, M_\theta) = \int_{-h(r)/2}^{h(r)/2} (\sigma_r, \sigma_\theta) z dz, \\ \rho_1 = \int_{-h(r)/2}^{h(r)/2} \rho(r) dz, \end{cases} \quad (14)$$

where it is clear in Eq. (13) that $N_r = N_r(r)$, $N_\theta = N_\theta(r)$, $M_r = M_r(r)$, $M_\theta = M_\theta(r)$ and $Q_r = Q_r(r)$. Therefore, the stress and moment resultants ($N_i, M_i, i = r, \theta$) and the shear stress resultants Q_r can be obtained with the use of Eqs. (9), (10) and (14) as follows:

$$\begin{cases} N_r = \frac{E(r)h(r)}{1-\nu^2} \left(\frac{du_0}{dr} + \frac{1}{2} \left(\frac{dw}{dr} \right)^2 + \nu \frac{u_0}{r} \right), \\ N_\theta = \frac{E(r)h(r)}{1-\nu^2} \left(\frac{u_0}{r} + \nu \frac{du_0}{dr} + \frac{\nu}{2} \left(\frac{dw}{dr} \right)^2 \right), \\ M_r = \frac{E(r)h^3(r)}{12(1-\nu^2)} \left(\frac{d\psi}{dr} + \nu \frac{\psi}{r} \right), \\ M_\theta = \frac{E(r)h^3(r)}{12(1-\nu^2)} \left(\frac{\psi}{r} + \nu \frac{d\psi}{dr} \right), \\ Q_r = \frac{k_s^2 E(r)h(r)}{2(1+\nu)} \left(\psi + \frac{dw}{dr} \right), \end{cases} \quad (15)$$

where $k_s^2 = 5/6$ is the shear-correction factor. Substituting the various terms from (15) into (13) yields a set of three non-linear

differential equations for the displacement field:

$$\begin{cases} E(r)h(r) \frac{d^2 u_0}{dr^2} + \left(\frac{dE(r)}{dr} h(r) + \frac{E(r)h(r)}{r} + E(r) \frac{dh(r)}{dr} \right) \frac{du_0}{dr} + \left(\frac{\nu h(r)dE}{r dr} - \frac{E(r)h(r)}{r^2} \right. \\ \left. + \frac{\nu E(r)dh(r)}{r dr} \right) u_0 + \left(\frac{dE(r)h(r)}{dr} + \frac{E(r)h(r)}{2r} + \frac{E(r)dh(r)}{2dr} \right) \left(\frac{dw}{dr} \right)^2 \\ + E(r)h(r) \left(\frac{dw}{dr} \right)^2 = -(1-\nu^2) \rho(r) h(r) r \omega^2, \\ \left(\frac{E(r)h^3(r)}{12(1-\nu^2)} \right) \frac{d^2 \psi}{dr^2} + \left(\frac{E(r)h^3(r)}{12(1-\nu^2)} + \frac{h^3(r)}{12(1-\nu^2)} \frac{dE(r)}{dr} + \frac{E(r)h^2(r)dh(r)}{4(1-\nu^2) dr} \right) \frac{d\psi}{dr} \\ + \left(\frac{\nu h^3(r)}{12(1-\nu^2)} \frac{dE(r)}{dr} - \frac{E(r)h^3(r)}{12r^2(1-\nu^2)} - \frac{k_s^2 E(r)h(r)}{2(1+\nu)} + \frac{\nu E(r)}{4r(1-\nu^2)} \frac{dh(r)}{dr} \right) \psi \\ - \left(\frac{k_s^2 E(r)h(r)}{2(1+\nu)} \right) \frac{dw}{dr} = 0, \\ \left(\frac{k_s^2 E(r)h(r)}{2(1+\nu)} \right) \frac{dw}{dr} + \left(\frac{k_s^2 E(r)h(r)}{2r(1+\nu)} + \frac{k_s^2 h(r)}{2(1+\nu)} \frac{dE(r)}{dr} + \frac{k_s^2 E(r)}{2(1+\nu)} \frac{dh(r)}{dr} \right) \psi \\ + \left(\frac{k_s^2 E(r)h(r)}{2(1+\nu)} \right) \frac{d^2 w}{dr^2} + \left(\frac{k_s^2 E(r)h(r)}{2r(1+\nu)} + \frac{k_s^2 h(r)}{2(1+\nu)} \frac{dE(r)}{dr} + \frac{k_s^2 E(r)}{2(1+\nu)} \frac{dh(r)}{dr} \right) \frac{dw}{dr} \\ + \frac{\nu E(r)h(r)du_0}{(1-\nu^2)r dr} + \frac{E(r)h(r)}{(1-\nu^2)r^2} u_0 + \frac{\nu E(r)h(r)}{2r(1-\nu^2)} \left(\frac{dw}{dr} \right)^2 - \rho_1 r \omega^2 \frac{dw}{dr} \\ + \left(\frac{E(r)h(r)du_0}{(1-\nu^2) dr} + \frac{E(r)h(r)}{2(1-\nu^2)} \left(\frac{dw}{dr} \right)^2 + \frac{\nu E(r)h(r)}{r(1-\nu^2)} u_0 \right) \frac{d^2 w}{dr^2} = -q. \end{cases} \quad (16)$$

It is worth mentioning that the difference between the present work and recent study done by Bayat et al. [16] is the direction of varying material properties which is along the radial direction in the present study. Hence, due to differences of material property and stiffness matrix, the non-linear equilibrium equations for the displacement field (Eq. (16)) are quite different from governing equations of Ref. [16]. Moreover, due to definition of $\rho(z)$ in [16] instead of $\rho(r)$ in the current study, the first moment of the density along the thickness does not exist in the force equilibrium equations (Eq. (13)).

To complete the formulation of the problem, the governing equations are accompanied by a set of boundary conditions. As shown in Fig. 1(b and c), the following two boundary conditions are employed [14,23]:

(a) Roller-supported solid disk (solid disk with a roller support at $r = r_o$):

$$\begin{cases} \text{at } r = 0, & u_0 = 0, \quad \psi = 0, \quad Q_r = 0, \\ \text{at } r = r_o, & w = 0, \quad N_r = 0, \quad M_r = 0. \end{cases} \quad (17)$$

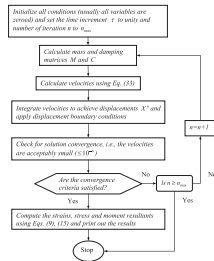
(b) Clamped-roller supported hollow disk (hollow disk with a clamped at the inner edge $r = r_i$ and roller supported at the outer edge $r = r_o$):

$$\begin{cases} \text{at } r = 0, & u_0 = 0, \quad \psi = 0, \quad Q_r = 0, \\ \text{at } r = r_o, & w = 0, \quad N_r = 0, \quad M_r = 0. \end{cases} \quad (18)$$

3. Numerical solution of the governing equations

The system of governing equations shows that the non-linear large deflection response of a functionally graded rotating disk under a bending load is very complex and is not amenable to a

closed form solution. Thus, using numerical procedures to obtain an approximate solution can be helpful. Several numerical solution methods are available, such as finite element, finite difference, finite strip, relaxation and the dynamic relaxation (DR) with the finite difference discretization method which was used here to solve the non-linear differential equations of the problem. Dynamic relaxation is an iterative method in which the basic idea is to transfer a static problem into a dynamic one [34]. The DR method is especially attractive for problems with highly non-linear geometric and material behavior. The explicit nature of this method makes it highly suitable for computers because all quantities may be treated as vectors, resulting in an easily programmed method with low storage requirements. Because of these advantages, many researchers have used the DR method to solve both linear and non-linear problems [35–38]. The DR flow chart is outlined briefly below.



According to the flow chart, all steps are thoroughly explained as following.

3.1. Initializing all condition

Generally at the first iteration, the initial vector values of approximate solution ($X_i^0 = \{u_i^0, \psi_i^0, w_i^0\}$) and all nodes velocities ($\dot{X}_i^0 = \{\dot{u}_i^0, \dot{\psi}_i^0, \dot{w}_i^0\}$) are defined to be zero (see [39,40]). It is clear that if iteration starts from an initial vector closer to the real solution, computation time will be reduced. Some studies are carried out to determine initial vector X^0 which is summarized in [40].

3.2. Computing the mass and damping matrices

Assume that with the aid of finite difference, a continuum subjected to a set of external forces has been transferred into an equivalent discrete system connected through N nodes ($i = 1, \dots, N$). The discrete governing equations of this static system can be written as

$$P(X^d) = F, \tag{19}$$

where $P_i = \{p_i^u, p_i^\psi, p_i^w\}$ is the vector of discrete internal forces, $X_i^d = \{u_i, \psi_i, w_i\}$ the vector of real solution of the discrete system and $F_i = \{f_i^u, f_i^\psi, f_i^w\}$ is the vector of discrete external forces. When the real solution (X^d) is replaced by an approximate solution X , residual forces $R = F - P(X)$ appear and in turn cause disequilibrium of the system. Hence, the corresponding dynamic equations are given as

$$M\ddot{X} + C\dot{X} + P(X) = F, \tag{20}$$

where M and C are fictitious mass and damping matrices and \dot{X} and \ddot{X} are velocity and acceleration vectors, respectively. The word ‘fictitious’ indicates that the dynamic process described by Eq. (20) is fictitious as the DR method is used so that M and C can be artificially chosen to obtain the static solution in a minimum number of pseudo-time increment steps. This enables one to construct Eq. (20) in such a way that M and C are diagonal matrices which simplify the investigation of the method to the

full extent. Hence, the DR algorithm is based on transforming a boundary value problem to an equivalent time-stepping initial value problem. Thus, for our analysis, the transformation of the disk equations into DR format was carried out by adding the damping and inertia terms to the right-hand-side of the force equilibrium Eq. (13) as follows:

$$\begin{cases} \frac{dN_r}{dt} + \frac{1}{r}(N_r - N_\theta) = m_u \frac{d^2 u_0}{dt^2} + c_u \frac{du_0}{dt} - \rho_1 r \omega^2, \\ \frac{dM_r}{dt} + \frac{1}{r}(M_r - M_\theta) - Q_r = m_\psi \frac{d^2 \psi}{dt^2} + c_\psi \frac{d\psi}{dt}, \\ \frac{dQ_r}{dt} + \frac{Q_r}{r} + N_r \frac{d^2 w}{dt^2} + \left(\frac{N_\theta}{r} - \rho_1 r \omega^2\right) \frac{dw}{dt} = m_w \frac{d^2 w}{dt^2} + c_w \frac{dw}{dt} - q. \end{cases} \tag{21}$$

where m_u, m_ψ, m_w and c_u, c_ψ, c_w are elements of the diagonal fictitious mass and damping matrices M and C , respectively. The mass matrix and nodal damping factor are defined in such a way to guarantee the stability and convergence of the iterative procedure. There are some methods which have been used in evaluating the element values of the fictitious mass matrix M (see [40]). Here, to guarantee the numerical stability, the element of matrix M is determined by the Gershgorin theorem as (for more detail see [41,42])

$$m_{ii}^l \geq .25(\tau^n)^2 \sum_{j=1}^N |k_{ij}^l|, \tag{22}$$

where $l : (u, \psi, w)$ and k_{ij} is the element of the stiffness matrix K and is computed by (see Appendix A):

$$K = \frac{\partial P}{\partial X}. \tag{23}$$

The relation between the elements of diagonal fictitious mass M and m_{ii}^l for a discrete system connected through N nodes is defined as follows:

$$M = \begin{bmatrix} m_{11} & 0 & \dots & 0 \\ 0 & m_{22} & \dots & 0 \\ \dots & \dots & \dots & \dots \\ 0 & 0 & \dots & m_{NN} \end{bmatrix}. \tag{24}$$

$$m_{ii} = \begin{bmatrix} m_{ii}^u & 0 & 0 \\ 0 & m_{ii}^\psi & 0 \\ 0 & 0 & m_{ii}^w \end{bmatrix}. \tag{25}$$

Similar relation between M and m_{ii}^l is used for elements of diagonal fictitious damping matrices C and c_{ii}^l . Proper selection of C can improve the convergence rate of the DR method. Five main approaches have been proposed in the published literature which is summarized in [40]. In this study, by applying the Rayleigh principle to each node, the instant critical damping factor for node i at the n th iteration expressed as [40]

$$c_i^n = 2 \left\{ \frac{(x_i^n)^T p_i^n}{(x_i^n)^T m_{ii}^n x_i^n} \right\}^{1/2}. \tag{26}$$

Therefore, different c values for different nodes are introduced to obtain the form used for DR as follows:

$$c_{ii} = c_i m_{ii}, \quad i = 1, \dots, N \tag{27}$$

It is notable that the governing equations for the displacement field (Eq. (16)) have very long terms. Thus, for the sake of brevity, Eq. (21) has been written based on force equilibrium equation (Eq. (13)). In our analysis, however, the developed numerical code is based on displacement equations (Eq. (16)) which can be attained by replacing the left-hand-sides of Eq. (21) with the left-hand-sides of Eq. (16). As mentioned, the left-hand-side of Eq. (21) is the vector of discrete internal forces, P , which is presented in complete form in Appendix A.

3.3. Determination of velocities and displacements

Eq. (20) is transformed to the explicit iterating formulae by replacing the velocity and acceleration terms with the following approximate central finite difference expressions:

$$\dot{X}^{n-(1/2)} = (X^n - X^{n-1})/\tau^n, \tag{28}$$

$$\ddot{X}^n = (\dot{X}^{n+(1/2)} - \dot{X}^{n-(1/2)})/\tau^n, \tag{29}$$

where τ is the increment of fictitious time at the n th iteration and in this work its value set to unity and the \dot{X}^n is obtained as following:

$$\dot{X}^n = \frac{1}{2}(\dot{X}^{n-(1/2)} + \dot{X}^{n+(1/2)}). \tag{30}$$

Substituting Eqs. (28)–(30) into Eq. (20) gives the following pair of equations to advance to the next velocity and displacement [40]:

$$\dot{X}_i^{n+(1/2)} = \frac{2\tau^n}{2 + \tau^n c_i^n} (m_{ii}^n)^{-1} r_i^n + \frac{2 - \tau^n c_i^n}{2 + \tau^n c_i^n} \dot{X}_i^{n-(1/2)}, \tag{31}$$

$$X_i^{n+1} = X_i^n + \tau^{n+1} \dot{X}_i^{n+(1/2)}, \tag{32}$$

where r_i^n is the residual vector of node i at the n th iteration.

Table 2
Material properties of FG disk used in the numerical study [14].

Material property	E (GPa)	ν	ρ (kg/m ³)
Partially stabilized zirconia (PSZ), ceramic	151.0	0.3	5700
Aluminum, metal	70.0	0.3	2700

Table 3
Comparison of maximum dimensionless deflection \bar{w}_{max} obtained by present study with those of Ma and Wang [45] for non-linear bending analysis of clamped and simply supported circular plate under different loadings.

$Q = \frac{qr_0^4}{D_0 h^3}$	\bar{w}_{max} of clamped circular plate		\bar{w}_{max} of simply supported circular plate	
	Ma and Wang [45]	Present solution	Ma and Wang [45]	Present solution
25	0.6622	0.6610	1.0502	1.0500
50	1.0340	1.0311	1.3741	1.3713
75	1.2941	1.2938	1.5965	1.5949
100	1.4666	1.4617	1.7659	1.7628
125	1.6394	1.6374	1.9024	1.8994
150	1.7772	1.7625	2.0213	2.0186

Table 4
Comparisons of the results ($\bar{w}_{max}^* = w/h$) obtained by the present solution with the results obtained by Turvey and Der Avanesian [46].

$\bar{q} = \frac{qr_0^4}{Eh^3}$	\bar{w}_{max}^* of clamped circular plate		\bar{w}_{max}^* of simply supported circular plate	
	Ref. [46]	Present solution	Ref. [46]	Present solution
5	0.7213	0.6917	0.9998	1.0521
10	1.0422	1.0502	1.3587	1.3630
15	1.2871	1.3013	1.5896	1.5963
20	1.4882	1.4961	1.7635	1.7695
25	1.6510	1.6544	1.8584	1.8612

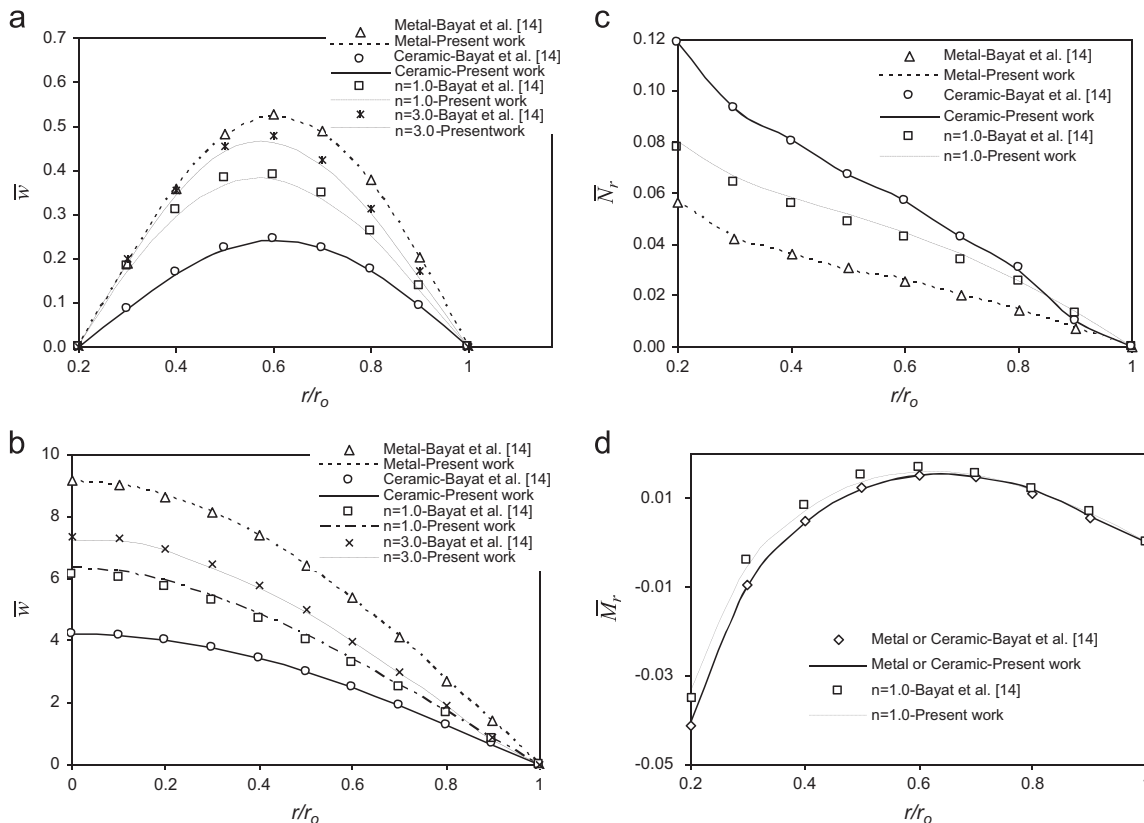


Fig. 3. Comparison of semi-analytical results [14] and the solutions reported here for the (a, b) dimensionless deflection \bar{w} and (c, d) dimensionless radial stress and moment resultant \bar{N}_r, \bar{M}_r , respectively, for FG solid (b) and hollow (a, c and d) rotating disks.

According to Eq. (21), the velocity equations are obtained as follows:

$$\begin{cases} \dot{u}_i^{n+(1/2)} = \frac{2r_i^n}{2+r_i^{2n}c_1^2}(m_{ii}^n)^{-1} \left(\frac{dN_r}{dr} + \frac{1}{r}(N_r - N_\theta) + \rho_1 r \omega^2 \right)_i^n + \frac{2-r_i^{2n}c_1^2}{2+r_i^{2n}c_1^2} u_i^{n-(1/2)}, \\ \dot{\phi}_i^{n+(1/2)} = \frac{2r_i^n}{2+r_i^{2n}c_1^2}(m_{ii}^n)^{-1} \left(\frac{dM_r}{dr} + \frac{1}{r}(M_r - M_\theta) - Q_r \right)_i^n + \frac{2-r_i^{2n}c_1^2}{2+r_i^{2n}c_1^2} \phi_i^{n-(1/2)}, \\ \dot{w}_i^{n+(1/2)} = \frac{2r_i^n}{2+r_i^{2n}c_1^2}(m_{ii}^n)^{-1} \left(\frac{dQ_r}{dr} + \frac{Q_r}{r} + N_r \frac{d^2w}{dr^2} + \left(\frac{N_\theta}{r} - \rho_1 r \omega^2 \right) \frac{dw}{dr} + q \right)_i^n + \frac{2-r_i^{2n}c_1^2}{2+r_i^{2n}c_1^2} w_i^{n-(1/2)}, \end{cases} \quad (33)$$

by integrating the velocities, the displacement vector, $X_i = \{u_i, \psi_i, w_i\}$, can be computed at the end of each time step according to Eq. (32).

3.4. Convergence criteria

The basic idea of DR is that the static solution of a mechanical system can be referred to as the steady state part of the transient response of the system to step loading [43]. Clearly at the steady state situation the values of velocity and residual vectors approach to zero. In the current study, the minimum kinetic energy ($\sum_j \dot{x}_j^{n+(1/2)} \leq 10^{-12}$) is used as the convergence criterion [40]. After computing the displacement field and applying the boundary conditions, strains and resultant stresses can be calculated.

To apply the DR method to solve the system of equations, they are discretized. Thus, a central finite difference technique was used to replace the derivatives. Due to the axisymmetric nature of the loading and the plate geometry, only a radial line of the plate is used, and the governing plate equations are applied to the nodal points of this line. Because of the singularity problem at the center, it is not possible to solve the equations at the center node of the plate. Therefore, the limiting process suggested by Kobayashi and

Turvey [44] was used. Consequently, Eqs. (31), (32), (3) and (15) and the appropriate boundary conditions and Eqs. (17) and (18) in their finite difference forms, constitute the set of equations for the sequential DR procedure.

4. Results and discussion

4.1. Verification of the solution

The accuracy and effectiveness of the present method for the linear and non-linear bending analyses of circular and annular isotropic or FG disks subjected to different loadings and boundary conditions were examined by three comparison studies as follow.

As a first part of validation of our methodology in linear bending analysis, the results of the numerical analysis for the axisymmetric small deflection bending of functionally graded solid and hollow rotating disks with roller and clamped-roller supported boundary conditions are compared with the semi-analytical results obtained by Bayat et al. [14]. In Ref. [14], a uniform thickness FG rotating disk with $r_o/r_i = 5$ and $r_o/h = 5$ subjected to a constant centrifugal force ($\omega = 1000$ rad/s) and transverse load ($q_o = 0.14$ GPa) was considered. Based on FSDT, the analysis was performed for one ceramic and metal combination. The material properties of zirconia (ceramic) and aluminum (metal) for the outer and inner surfaces of the FG rotating disk are given in Table 2. The results were plotted in a non-dimensional form for the deflection \bar{w} , radial stress and moment resultants \bar{N}_r , \bar{M}_r , respectively. According to Fig. 3(a–d), the results are in good agreement with those given in [14], and the validity of the numerical method is verified.

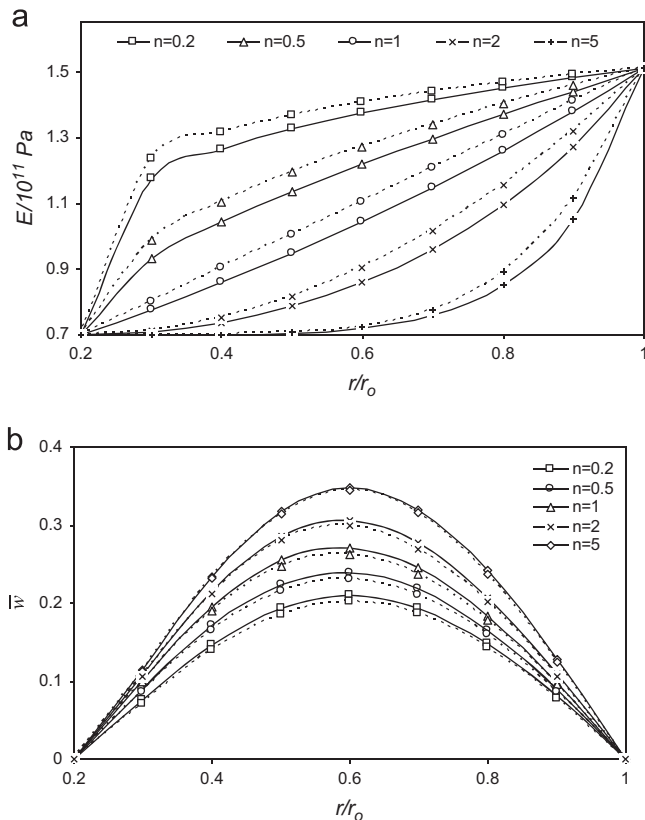


Fig. 4. Effects of the distribution rule (Mori–Tanaka scheme and a simple power law) on (a) the effective Young’s modulus, E , and (b) the dimensionless deflection, \bar{w} , along the radius of an FG hollow rotating disk. The dashed lines denote the simple power law distribution.

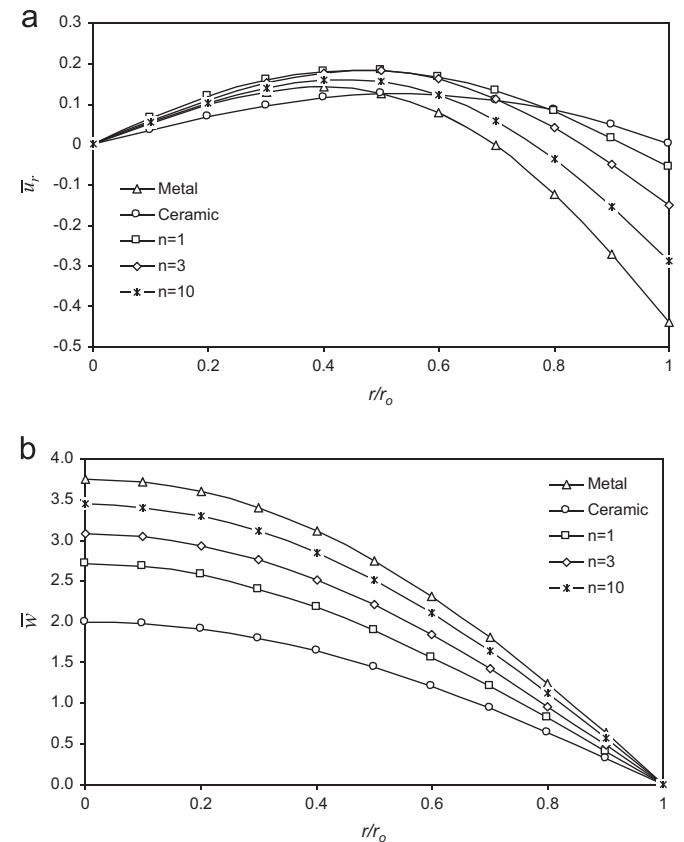


Fig. 5. Effects of the grading index n on the (a) dimensionless radial displacement, \bar{u} , and (b) dimensionless deflection, \bar{w} , along the radius of a FG solid rotating disk.

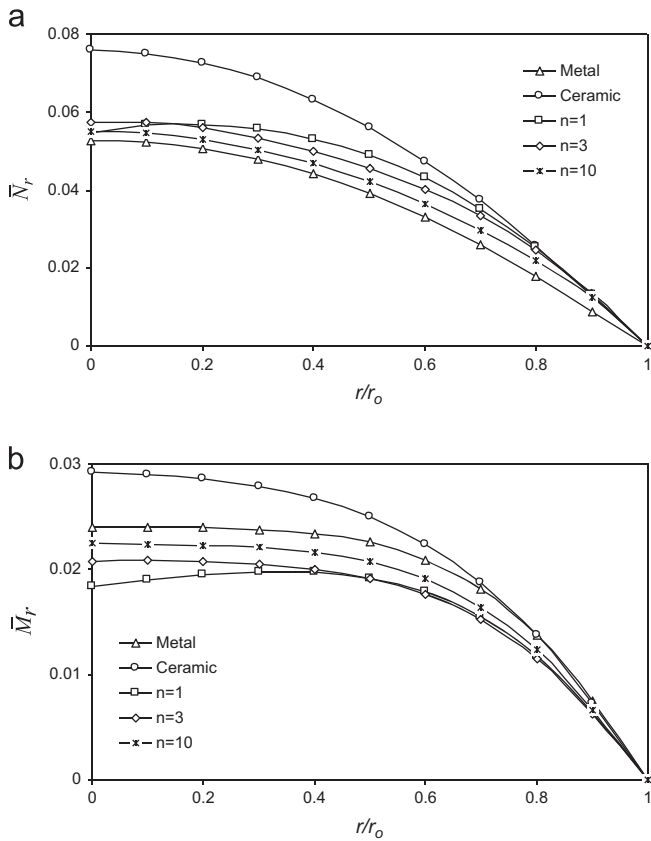


Fig. 6. Effects of the grading index n on the (a) dimensionless radial stress resultant, \bar{N}_r , and (b) dimensionless radial moment resultant, \bar{M}_r , along the radius of an FG solid rotating disk.

As the next example, comparisons of the numerical results obtained in the present paper with those reported by Ma and Wang [45] for an axisymmetric large deflection bending problem of a circular plate with clamped and simply supported boundary conditions are shown in Tables 3 and 4. For the dimensionless maximum deflection $\bar{w}_{\max} = 64w_{\max}D_c/qr_0^4$ with $D_c = Ec h^3/12(1-\nu^2)$, a good agreement was observed.

As a final part of our analysis verification, the DR results for the axisymmetric non-linear bending problem of a circular plate under different mechanical loadings with clamped and simply supported boundary conditions are compared in Table 4 with the numerical results obtained by Turvey and Der Avanesian [46]. It is obvious that the present results for dimensionless maximum deflection $\bar{w}_{\max}^* = w/h$ are in good consistency with those given in Ref. [46]. It can be seen that the results obtained by the present method are in close agreements with those obtained by other investigators. Hence, the reliability and accuracy of the present method are verified.

4.2. Parametric study

Using FSDT, a parametric study was carried out to investigate the non-linear bending of shear deformable functionally graded rotating disks with uniform and variable thicknesses subjected to constant centrifugal forces and transverse uniform loads as shown in Fig. 1. For the numerical study, two cases were considered, namely roller-supported solid disks and clamped-roller supported (CR) hollow disks. The analysis was conducted using aluminum as the inner surface metal and zirconia as the outer surface ceramic, as specified in Table 2. The results presented herein are for a specified thickness-to-external radius ratio of the FG disk ($h/r_0 = 0.15$) with a material constant $n=1$, under a uniform centrifugal force due to a uniform rotating speed ($\omega = 500$ rad/s)

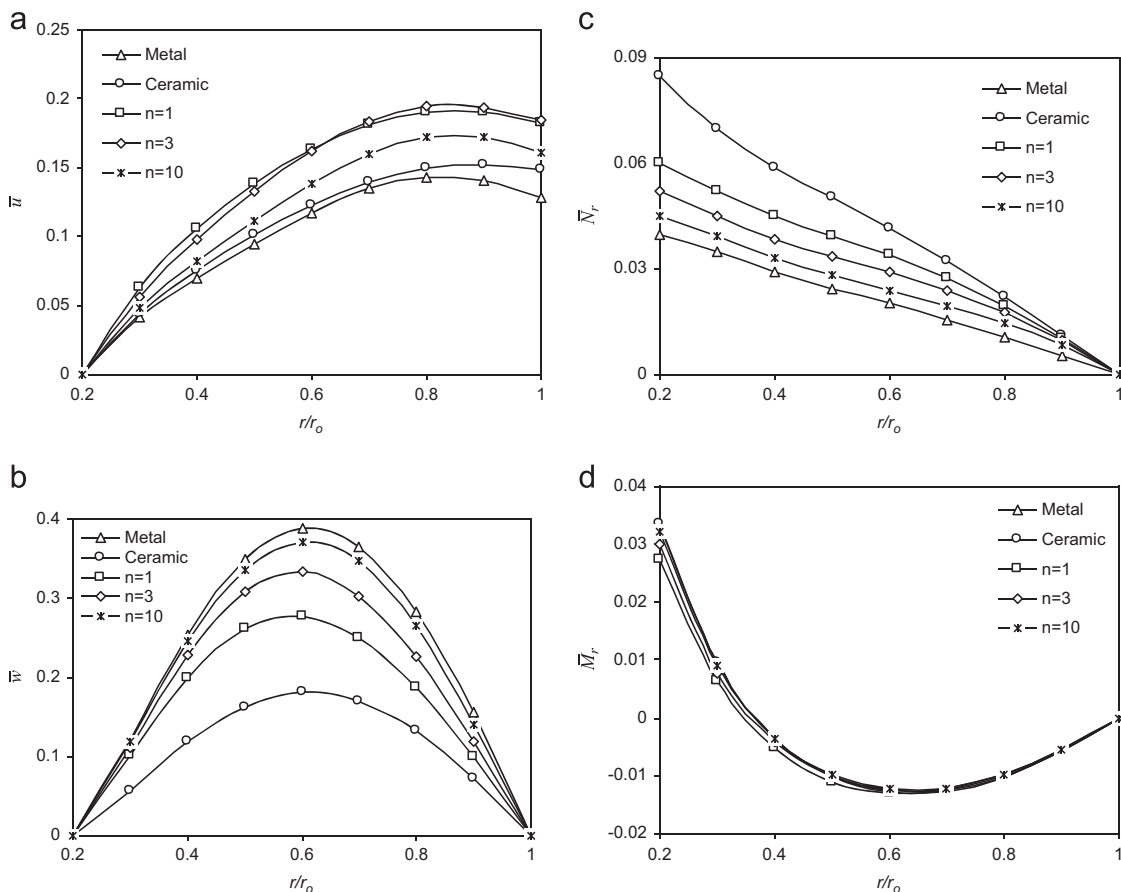


Fig. 7. Effects of the grading index, n , on the (a) dimensionless radial displacement, \bar{u}_r , (b) dimensionless deflection, \bar{w} , (c) dimensionless radial stress resultant, \bar{N}_r , and (d) dimensionless radial moment resultant, \bar{M}_r , along the radius of an FG hollow rotating disk.

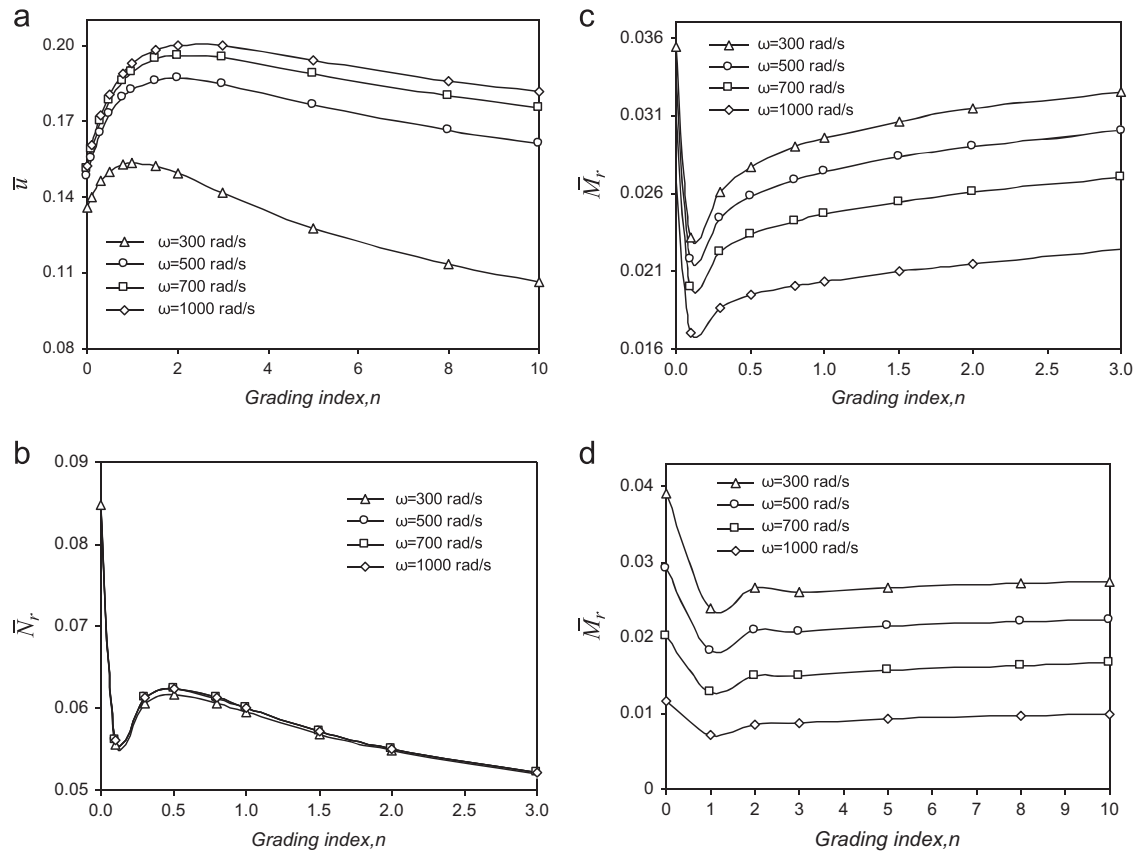


Fig. 8. Effects of the grading index, n , on the (a) dimensionless radial displacement, \bar{u} , at the outer radius, (b) maximum dimensionless radial stress resultant, \bar{N}_r , and (c, d) the maximum dimensionless radial moment resultant, \bar{M}_r , for FG hollow (a, b and c) and solid (d) disks with different rotating speeds.

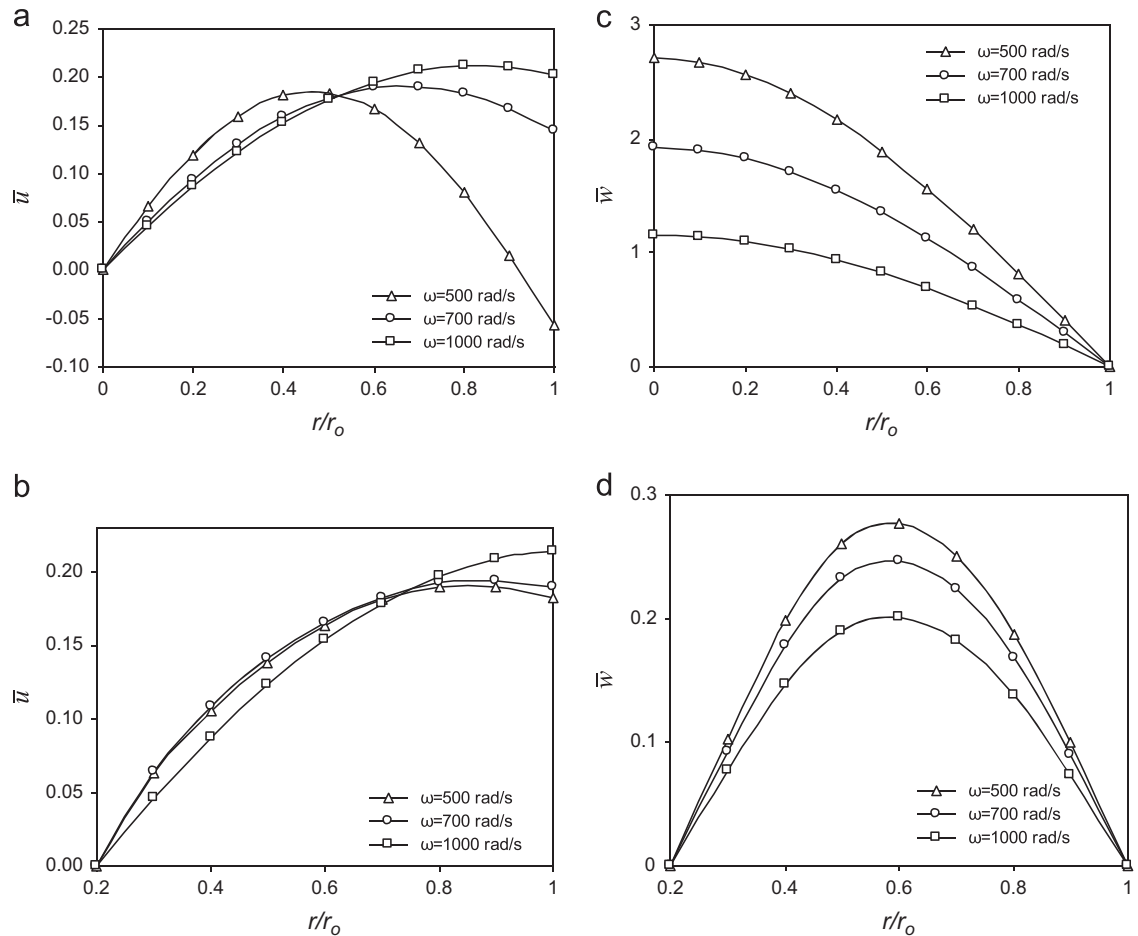


Fig. 9. Effects of the angular velocity, ω , on the (a, b) dimensionless radial displacement, \bar{u} , and (c, d) dimensionless deflection, \bar{w} , along the radius of FG solid (a, c) and hollow (b, d) rotating disks with $n=1$.

and transverse load ($q = 140$ MPa) on the top surface, unless stated otherwise. Moreover, the ratio of the outer radius-to the-inner radius of the hollow disk was assumed to be $r_o/r_i = 5$, and for both solid and hollow disks, the outer radius was $r_o = 50$ mm. As shown in Fig. 2, three different thickness profiles were considered to study the effect of thickness variation. The results are defined and presented in terms of the following dimensionless quantities, $\bar{w} = 64wD_c/qr_o^4$ with $D_c = E_c h^3/12(1-\nu^2)$, $\bar{z} = z/h$, $\bar{u} = u_r E_c/\rho_c \omega^2 r_o^3$, $\bar{\sigma}_r = \sigma_r/E_c$, $\bar{\sigma}_\theta = \sigma_\theta/E_c$, $\bar{N}_r = N_r/\rho_c r_o^3 \omega^2$ and $\bar{M}_r = M_r/\pi r_o^2 q$, which are the dimensionless deflection (vertical displacement), distance from middle plane, radial displacement, radial and circumferential equivalent stresses, radial stress resultant and radial moment resultant, respectively. The Mori-Tanaka theory was used to model the FGM material properties. A study was conducted to compare the Mori-Tanaka theory with the simple rule of mixture. The variations of Young's modulus E and the dimensionless deflection \bar{w} are represented in Fig. 4(a) and (b), respectively, for both rules of mixture for a hollow FG rotating disk under a bending load with different values of the grading index n . There was some differences between the results obtained using the two methods. Therefore, to obtain more realistic prediction for the behavior of the FG disk, the Mori-Tanaka scheme was used in the following results.

In Fig. 5a, the influence of the grading index n on the variation of the dimensionless radial displacement \bar{u} along the radius is demonstrated. For different values of the grading index n , the radial displacement has a maximum at $r/r_o = 0.5$ for FG rotating disks. For the ceramic disk, \bar{u} is positive along the radius. However, in FG and metallic disks, \bar{u} becomes negative for some values of r , due to the combined effect of the centrifugal and bending loads. For instance, the

effect of the bending load compared to the centrifugal force becomes dominant after $r/r_o > 0.7$ for a metallic disk. Furthermore, the higher values of the grading index n cause the radial displacement to become more negative in the outer parts of the disks, and the absolute value of \bar{u} for $n=10$ is about five times greater than that for $n=1$.

Fig. 5b illustrates variations of the dimensionless deflection \bar{w} along the radius of an FG solid rotating disk for different values of the grading index n . As expected, by increasing the grading index n and consequently decreasing the stiffness, the deflections increase so that the maximum dimensionless deflection of the fully metallic disk is nearly twice of that of the fully ceramic one.

Fig. 6a and b indicates the variations of dimensionless radial stress and moment resultants \bar{N}_r and \bar{M}_r along the radius of the FG solid rotating disk for different values of the grading index n , respectively. The fully ceramic disk has the maximum values of \bar{N}_r . Higher values of n reduce \bar{N}_r so that the value of \bar{N}_r at the center of the fully ceramic disk is about 44% larger than that for the fully metallic disk. Furthermore, using larger values of n in FG rotating disks increases the \bar{M}_r . Moreover, the value of \bar{M}_r in the fully ceramic disk is greater than that for the fully metallic one, see Fig. 6b. The form of the variation of \bar{M}_r for non-homogenous FG disks is different and it does not vary with n monotonically, as discussed later in detail.

Fig. 7a demonstrates the variation of \bar{u} along the radius for different values of the grading index n for FG hollow rotating disks. The homogenous metallic and ceramic disks have lower amounts of \bar{u} , whereas the FG disks have greater values. In fact, the variation of \bar{u} with the grading index n is also not monotonic.

Fig. 7b illustrates the variation of \bar{w} along the radius for different values of the grading index n for the hollow disk. As aforementioned, increasing the n results in greater deflection

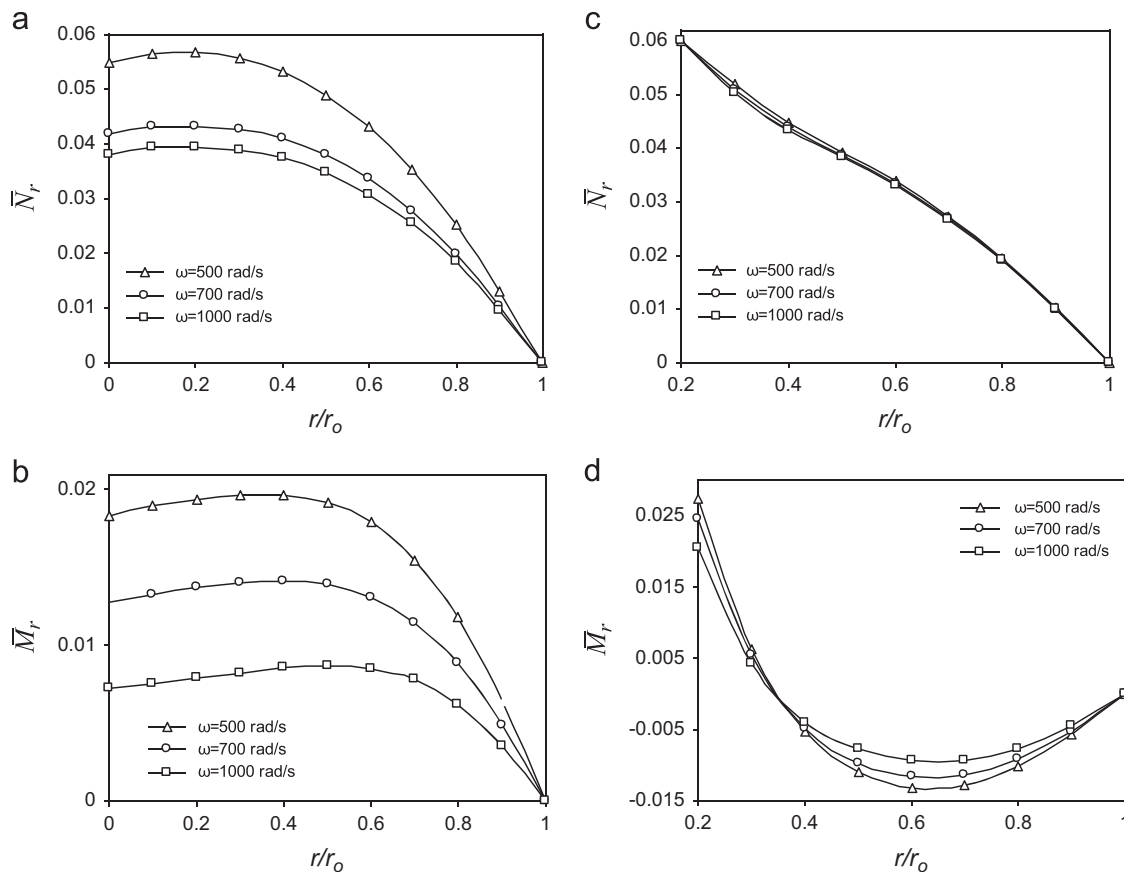


Fig. 10. Effect of the angular velocity, ω , on the (a, c) dimensionless radial stress resultant, \bar{N}_r , and (b, d) dimensionless radial moment resultant, \bar{M}_r , along the radius of FG solid (a, b) and hollow (c, d) rotating disks with $n=1$.

so that the maximum deflection of a fully metallic disk is about twice of that of the ceramic one. Moreover, increasing n causes a reduction of \bar{N}_r which can be attributed to the reduction of the strain values of FG disks, see Fig. 7c.

Fig. 7d shows the variation of \bar{M}_r along the radius of the FG hollow disk. The maximum of \bar{M}_r occurs at the inner radius of both homogenous metallic and ceramic disks. Moreover, the maximum values of \bar{M}_r for the non-homogenous FG disks are not located between the metallic and ceramic ones.

To explore some of previous occurrences, the variations of some parameters with the grading index n are given in Fig. 8. Fig. 8a shows the variation of \bar{u} versus n at the outer radius of the FG hollow disk for different values of the rotating speed. The parameter \bar{u} has a maximum at $n=1$ for $\omega=300$ rad/s. However, by increasing the rotating speed the location of the maximum points approaches $n=2$. By increasing n , \bar{u} decreases and approaches its value for the homogenous metallic disk.

The variations of the maximum of \bar{N}_r and $(\bar{N}_r)_{\max}$ (at the inner radius of the FG hollow disk) for different values of the grading index n and rotating speed are given in Fig. 8b. The value of $(\bar{N}_r)_{\max}$ decreases with increasing grading index from $n=0$ to 0.1. After that, there is an increase for $(\bar{N}_r)_{\max}$ from $n=0.1$ to 0.5. Finally, with increasing n from $n=0.5$ to larger values and the tendency of the material toward the homogenous metallic disk, the $(\bar{N}_r)_{\max}$ decreases again. The value of $(\bar{N}_r)_{\max}$ for the FG rotating disk is always between the values for the homogenous metallic and ceramic disks. In addition, the effect of the rotating speed ω on $(\bar{N}_r)_{\max}$ is not significant.

The variations of \bar{M}_r at the inner radius of the FG hollow disk for different values of n and rotating speeds are shown

in Fig. 8c. The minimum of \bar{M}_r occurs for $n=0.1$ for different rotating speeds. Moreover, the values of \bar{M}_r of the FG rotating disks are not between those of the homogenous ceramic and metallic disks.

Fig. 8d illustrates the variations of \bar{M}_r at the center of the FG solid disk for different values of n and rotating speeds. The minimum of \bar{M}_r always occurs for $n=1$ and for the grading index between zero and one it decreases. Moreover, beyond $n=2$, \bar{M}_r varies with the grading index very slightly.

Fig. 9 shows the effect of the centrifugal force caused by the angular velocity ω on the dimensionless vertical and radial

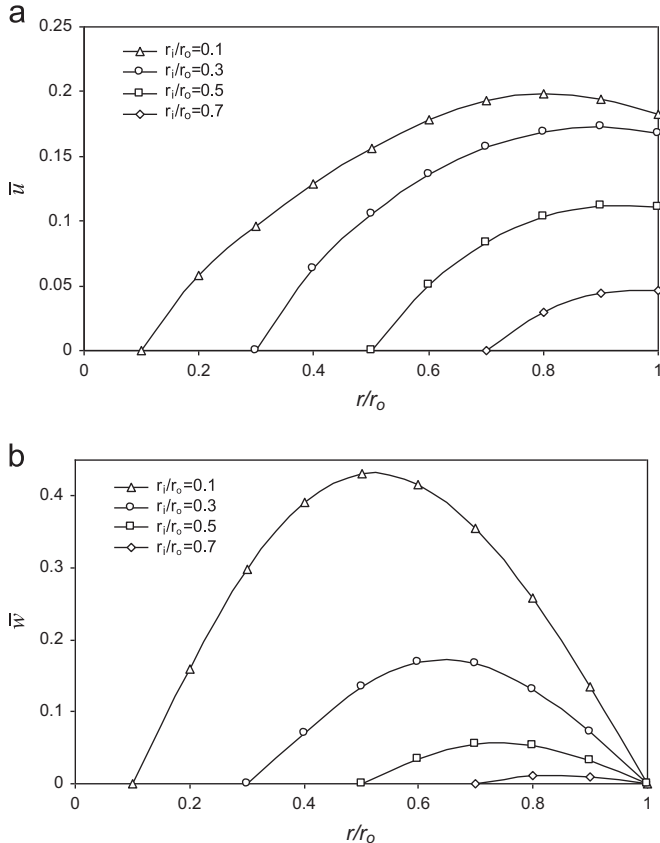


Fig. 11. Effects of the inner radius-to-outer radius ratio, r_i/r_o , on the (a) dimensionless radial displacement, \bar{u} , and (b) dimensionless deflection, \bar{w} , along the radius of an FG hollow rotating disk with $n=1$.

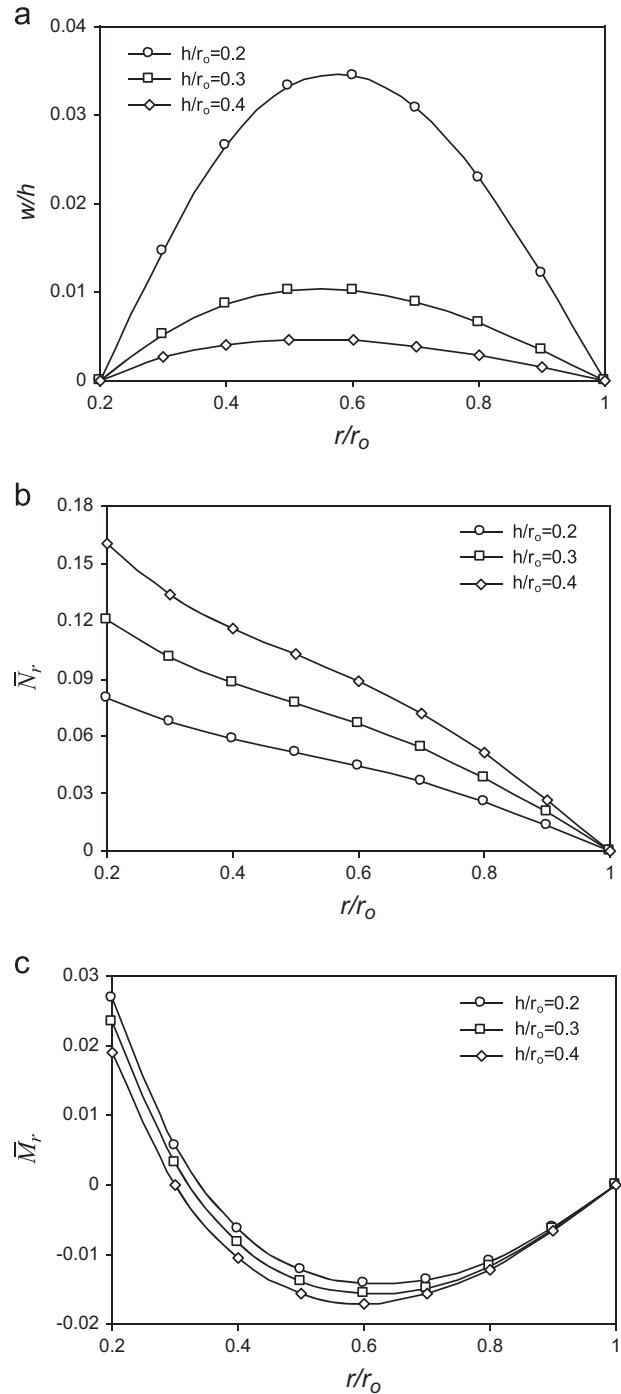


Fig. 12. Effects of thickness radius ratio, h/r_o , on the (a) normalized deflection, w/h , (b) dimensionless radial stress resultant, \bar{N}_r , and (c) dimensionless radial moment resultant, \bar{M}_r , along the radius of an FG hollow rotating disk with $n=1$.

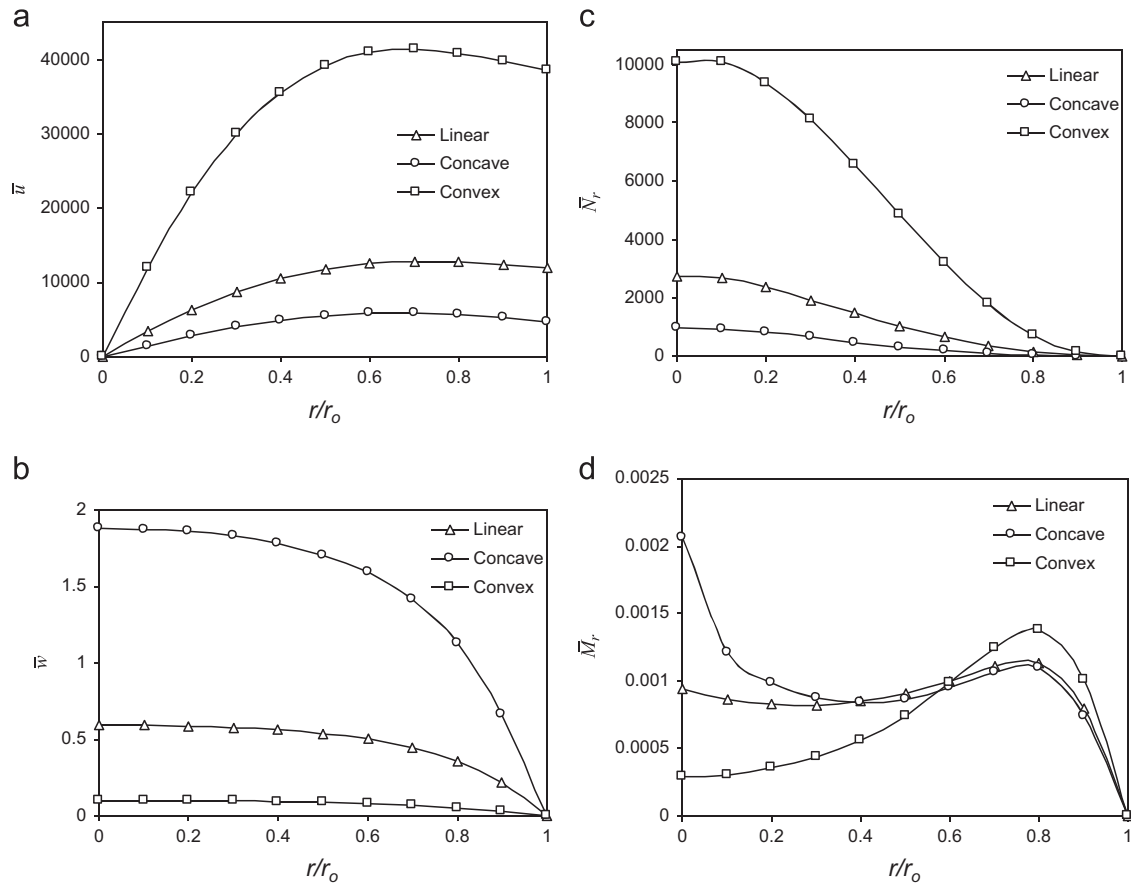


Fig. 13. Effects of the thickness profile (linear, concave and convex) on (a) the dimensionless radial displacement, \bar{u}_r , (b) dimensionless deflection, \bar{w} , (c) dimensionless radial stress resultant, \bar{N}_r , and (d) dimensionless radial moment resultant, \bar{M}_r , along the radius of an FG solid rotating disk with $n=1$ and $\omega = 10$ rad/s.

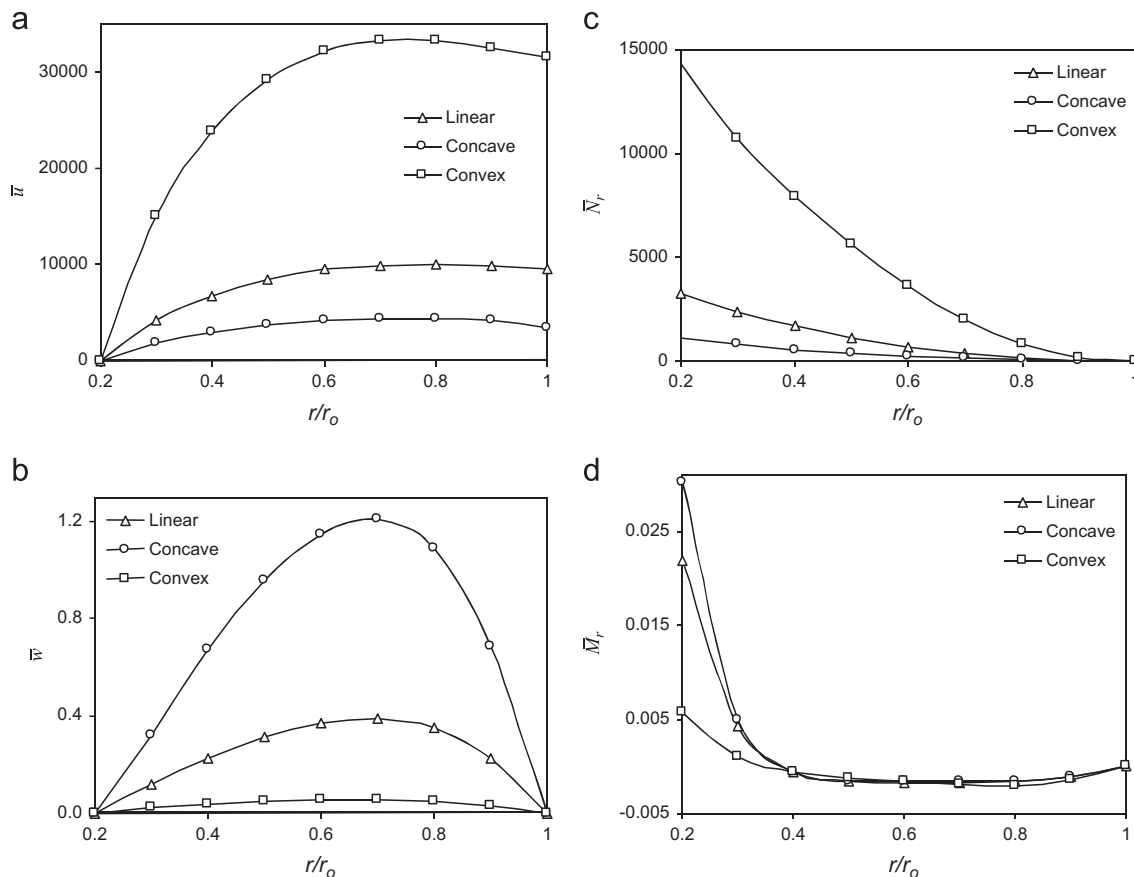


Fig. 14. Effects of the thickness profile (linear, concave and convex) on the (a) dimensionless radial displacement, \bar{u}_r , (b) dimensionless deflection, \bar{w} , (c) dimensionless radial stress resultant, \bar{N}_r , and (d) dimensionless radial moment resultant, \bar{M}_r , along the radius of an FG hollow rotating disk with $n=1$ and $\omega = 10$ rad/s.

displacements. Fig. 9a and b shows the variation of \bar{u} for different angular velocities for FG solid and hollow rotating disks, respectively. In addition, the variations of \bar{u} along the radius of the solid disks for $\omega = 500$ rad/s and $\omega = 1000$ rad/s are very different. For $\omega = 500$ rad/s, \bar{u} has a maximum at $r/r_0 = 0.4$ and encounters a sharp decrease after that point. For $\omega = 1000$ rad/s, the maximum occurs at $r/r_0 = 0.8$ and then there is a smooth decrease, see Fig. 9a. For the hollow disk, however, \bar{u} has a maximum at $r/r_0 = 0.8$ for $\omega = 500$ rad/s, and the maximum of \bar{u} occurs at the outer radius of the disk for $\omega = 1000$ rad/s. The behavior of \bar{u} at lower rotating speeds can be attributed to the dominance of the bending load over the centrifugal force.

The effects of the rotating speed on the variations of the dimensionless deflection \bar{w} along the radius of the FG solid and hollow rotating disks are considered in Fig. 9c and d, respectively. Fig. 9c and d shows that the accelerating angular velocity reduces the deflection of the solid and hollow disks so that the central deflection of the solid disk at $\omega = 1000$ rad/s is nearly half of that at $\omega = 500$ rad/s.

Fig. 10a and b shows the variation of \bar{N}_r and \bar{M}_r along the radius of the solid disk for different values of ω . Increasing of ω decreases \bar{N}_r and \bar{M}_r along the radius so that their values for $\omega = 500$ rad/s at the center of the disk are almost 1.5 and 2.5 times greater than those for $\omega = 1000$ rad/s, respectively.

Similarly, Fig. 10c and d shows the effect of the angular velocity ω on the variation of \bar{N}_r and \bar{M}_r along the radius of the hollow disk. For the hollow disk, the values of \bar{N}_r for different velocities are very close to each other, see Fig. 10c. In contrast, \bar{M}_r reaches a maximum at the inner edge of the disk and its absolute value decreases as ω increases, see Fig. 10d.

Fig. 11a and b shows the influences of the inner radius-to-outer radius ratio, r_i/r_0 , on the values of \bar{u} and \bar{w} , respectively. As expected, increasing r_i/r_0 causes a decrease of the maximum radial displacement of \bar{u} and the maximum deflection of \bar{w} . In fact, the maximum values of \bar{u} and \bar{w} at $r_i/r_0 = 0.1$ are about 1.8 and 8 times larger than those at $r_i/r_0 = 0.5$, respectively.

Fig. 12a–c shows the effect of the thickness radius ratio, h/r_0 , on the variation of the normalized deflection, w/h , the dimensionless radial stress resultant, \bar{N}_r , and the dimensionless radial moment resultant, \bar{M}_r , along the radius of the FG hollow rotating disk with $n=1$, respectively. An increase in the deflection occurs when the thickness decreases. For instance, the maximum deflection of the hollow disk with $h/r_0 = 0.2$ is much greater than that with the $h/r_0 = 0.4$. Moreover, unlike \bar{M}_r , reducing the thickness causes a decrease of \bar{N}_r . For example, the maximum value of \bar{N}_r at $h/r_0 = 0.4$ is about twice that at $h/r_0 = 0.2$, see Fig. 12b and c.

The effect of different thickness profiles (linear, concave and convex) on \bar{u} , \bar{w} , \bar{N}_r and \bar{M}_r of an FG solid disk with $n=1$ and $\omega = 10$ rad/s is shown in Fig. 13. It is clear that the maximum and minimum values of \bar{u} occur for the convex and concave profiles, respectively, see Fig. 13a. Moreover, as expected, the plates with concave and convex profiles have the maximum and minimum deflections for a FG solid disk with $n=1$, respectively. For instance, the central deflection of the FG solid disk with the concave profile is about 18.3 times that for the convex profile, see Fig. 13b. Furthermore, the maximum and minimum values of \bar{N}_r along the radius occur for the convex and concave profiles, respectively, see Fig. 13c. The value of \bar{N}_r at the center of an FG solid rotating disk with a convex profile for $n=1$ is about 10.4 and 3.6 times larger than the same values with concave and linear profiles, respectively. In addition, the maximum values of \bar{M}_r occur for the concave thickness profile. The maximum values of \bar{M}_r for the concave thickness profile are about 7 and 2 times larger than those of the convex and linear thickness profiles, respectively, see Fig. 13d.

Fig. 14 illustrates the variations of \bar{u} , \bar{w} , \bar{N}_r , and \bar{M}_r with different thickness profiles of FG hollow rotating disks with $n=1$ and

$\omega = 10$ rad/s. Similar to solid disks, the maximum and minimum values of \bar{u} for the FG hollow rotating disks occur for the convex and concave profiles, respectively, see Fig. 14a. The maximum deflection of the hollow FG rotating disk with a concave thickness profile is about 20 and 3 times greater than those of the convex and linear profiles, respectively, see Fig. 14b. Moreover, the difference between the values of \bar{N}_r and \bar{M}_r for the different profiles is shown in Fig. 14c and d. The maximum of \bar{N}_r , which occurs at the inner edge of the disk with a convex profile, is about 13.3 and 4.3 times greater than those of the concave and linear profiles, respectively. Finally, the maximum \bar{M}_r occurs at the inner radius of the hollow disk with a concave profile and is nearly equal to that of the linear profile, but it is more than five times larger of

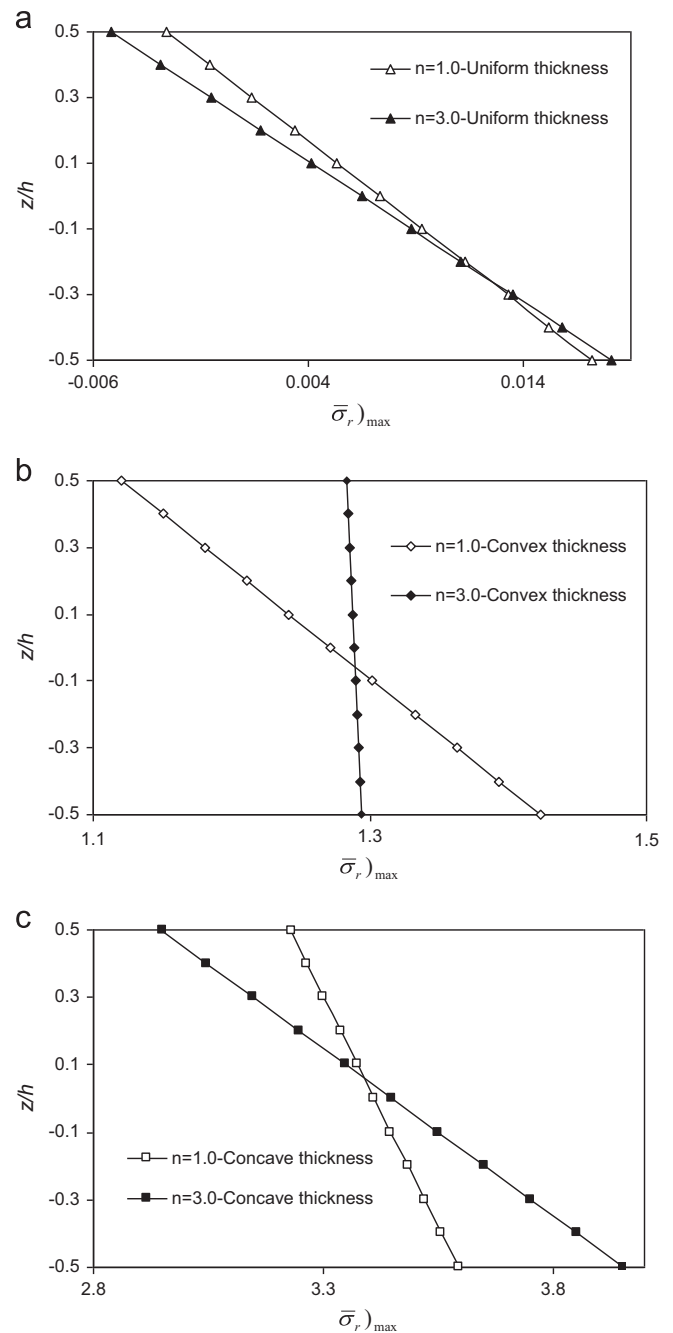


Fig. 15. Effects of the grading index, n , and thickness profile (uniform (a), convex (b) and concave (c)) on the maximum dimensionless radial equivalent stress, $(\bar{\sigma}_r)_{\max}$, through the thickness of an FG hollow rotating disk.

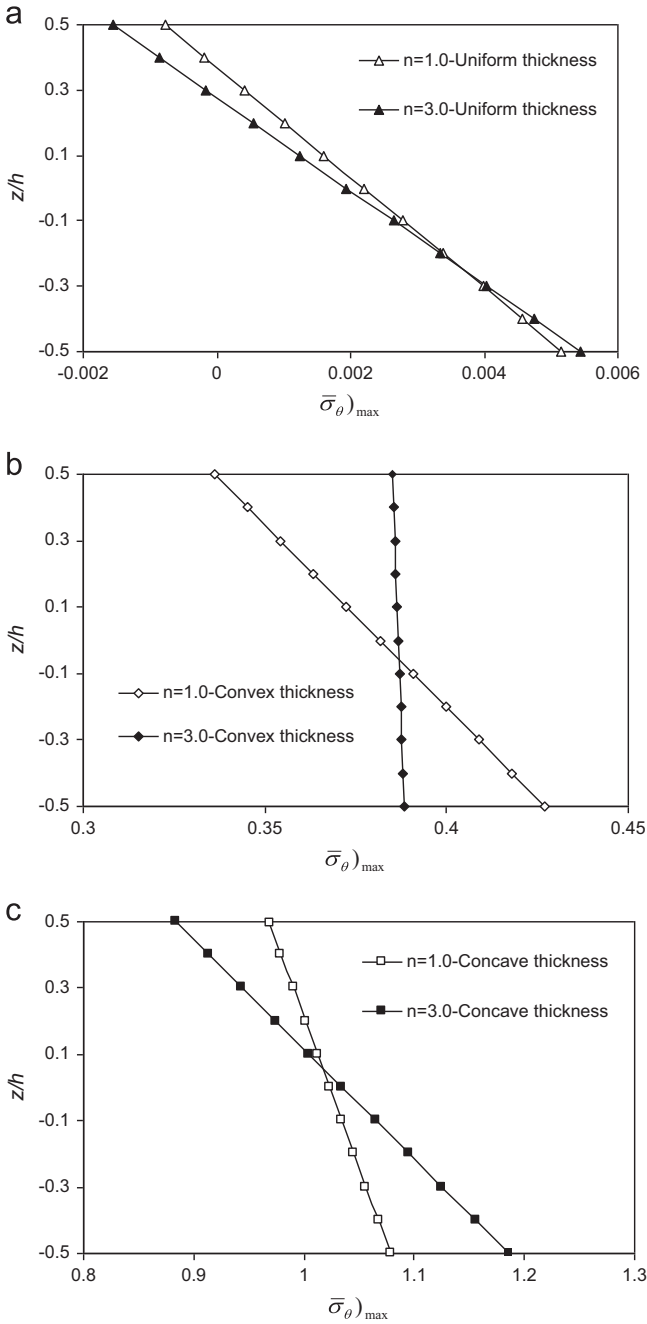


Fig. 16. Effects of the grading index, n , and thickness profile (uniform (a), convex (b) and concave (c)) on the maximum dimensionless circumferential equivalent stress, $(\bar{\sigma}_\theta)_{max}$, through the thickness of an FG hollow rotating disk.

the convex profile. Beyond $r/r_0 = 0.4$, the change of \bar{M}_r for different thickness profiles is not significant.

Finally, because of the dependency of equivalent stresses $(\bar{\sigma}_r, \bar{\sigma}_\theta)$ to the both radial and thickness directions, the critical stresses are considered along thickness of the inner radius of FG hollow rotating disk. Variations of maximum $\bar{\sigma}_r$ and $\bar{\sigma}_\theta$ for two different grading indices $n=1, 3$ and different types of thickness profiles (uniform, convex and concave) along the thickness of inner radius of FG hollow rotating disk are showed in Figs. 15 and 16, respectively. It is clear that $\bar{\sigma}_\theta$ has smaller absolute values compared to $\bar{\sigma}_r$. Moreover, at the upper and bottom surfaces of uniform thickness profile, the maximum values of equivalent stresses $(\bar{\sigma}_r$ and $\bar{\sigma}_\theta)$ are tensile and compressive, respectively. While, $\bar{\sigma}_r$ and $\bar{\sigma}_\theta$ possess positive values at the inner radius of FG

hollow rotating disk with variable thickness so that the maximum value of tensile stress related to concave thickness profile. Moreover, it is observable that unlike the convex thickness profile, the more material gradient index n leads to the more absolute values of $\bar{\sigma}_r$ and $\bar{\sigma}_\theta$ at the upper and bottom surfaces of FG rotating disk.

5. Conclusions

The non-linear bending analysis of FG rotating solid and hollow disks with uniform and variable thicknesses was studied. Based on FSDT and using the von-Karman theory for large deflections, the non-linear equilibrium equations were developed and a dynamic relaxation method combined with a finite difference discretization technique was used to solve these equations. The effects of the grading index parameter, angular velocity, geometry, thickness-to-radius ratio and thickness profile of the disk were studied. Some general inferences are given below:

- It was shown that \bar{u} has a maximum at the outer radius of the hollow disk at $n=1$ for $\omega = 300$ rad/s, and by increasing the rotating speed to $\omega = 500, 700$ and 1000 rad/s, the maximum values occur at $n=2$.
- The maximum of \bar{N}_r for the hollow FG disk decreases by increasing the grading index from $n=0$ to 0.1 and then increases from $n=0.1$ to 0.5 . Then, with increasing n from $n=0.5$ and the tendency toward the homogenous metallic disk, the maximum of \bar{N}_r decreases.
- The minimum value of \bar{M}_r in inner radius of the FG hollow disk occur at $n=0.1$; however, at the center of the FG solid disk, \bar{M}_r has a minimum value at $n=1$.
- The central deflection of the solid disk at $\omega = 1000$ rad/s is less than half of that at $\omega = 500$ rad/s.
- Increasing ω leads a decrease in \bar{M}_r (absolute value) in the FG solid and hollow rotating disks. Moreover, for the FG hollow disk, the effect of the angular velocity on \bar{N}_r along the radius is not significant. Furthermore, increasing ω leads to a decrease in \bar{N}_r for solid disks.
- Different behaviors for \bar{M}_r and the maximum and minimum values of \bar{N}_r along the inner radius were found for the convex and concave profiles.

Appendix A

As mentioned, $p_i = \{p_i^u, p_i^v, p_i^w\}$ ($i = 1, \dots, N$) is the vector of discrete internal forces for each node so that $P = \{p_1, \dots, p_i, \dots, p_N\}^T$ is defined for the equivalent discrete system connected through N nodes. The complete form of p_i is expressed in the left-hand-side of the Eq. (21) based on stress and moment resultants

$$\begin{cases} p_i^u = \left(\frac{dN_r}{dr}\right)_i + \frac{1}{r_i}((N_r)_i - (N_\theta)_i), \\ p_i^v = \left(\frac{dM_r}{dr}\right)_i + \frac{1}{r_i}((M_r)_i - (M_\theta)_i) - (Q_r)_i, \\ p_i^w = \left(\frac{dQ_r}{dr}\right)_i + \frac{(Q_r)_i}{r_i} + (N_r)_i \left(\frac{d^2 w}{dr^2}\right)_i + \left(\frac{N_\theta}{r} - \rho_1 r \omega^2\right)_i \left(\frac{dw}{dr}\right)_i. \end{cases} \quad (A.1)$$

In the current numerical code, Eq. (A.1) is defined based on displacement field by substituting Eq. (15) into Eq. (A.1) which is the left-hand-side of Eq. (16). According to Eqs. (A.1) and (23), the stiffness matrix K (3×3) can be defined for each node and

iteration as follows:

$$K = \begin{bmatrix} \frac{\partial p^u}{\partial u} & \frac{\partial p^u}{\partial \psi} & \frac{\partial p^u}{\partial w} \\ \frac{\partial p^w}{\partial u} & \frac{\partial p^w}{\partial \psi} & \frac{\partial p^w}{\partial w} \\ \frac{\partial p^w}{\partial u} & \frac{\partial p^w}{\partial \psi} & \frac{\partial p^w}{\partial w} \end{bmatrix}, \quad (\text{A.2})$$

$$K_{11} = \frac{\partial p^u}{\partial u} = E(r)h(r) \frac{d^3 u}{dr^3} + \left(\frac{dE(r)}{dr} h(r) + \frac{E(r)h(r)}{r} + E(r) \frac{dh(r)}{dr} \right) \frac{d^2 u}{dr^2} + \left(\frac{\nu h(r)dE}{r dr} + \frac{E(r)h(r)}{r^2} + \frac{\nu E(r)dh(r)}{r dr} \right) \frac{du}{dr}, \quad (\text{A.3})$$

$$K_{12} = \frac{\partial p^u}{\partial \psi} = 0, \quad (\text{A.4})$$

$$K_{13} = \frac{\partial p^u}{\partial w} = 2 \left(\frac{dE(r)h(r)}{dr} + \frac{E(r)h(r)}{2r} (1-\nu) + \frac{E(r)dh(r)}{2 dr} \right) \frac{dw d^2 w}{dr dr^2} + E(r)h(r) \left(\frac{d^2 w d^2 w}{dr^2 dr^2} \right) + E(r)h(r) \left(\frac{dw d^3 w}{dr dr^3} \right), \quad (\text{A.5})$$

$$K_{21} = \frac{\partial p^w}{\partial u} = 0, \quad (\text{A.6})$$

$$K_{22} = \frac{\partial p^w}{\partial \psi} = \left(\frac{E(r)h^3(r)}{12(1-\nu^2)} \right) \frac{d^3 \psi}{dr^3} + \left(\frac{E(r)h^3(r)}{12r(1-\nu^2)} + \frac{h^3(r)}{12(1-\nu^2)} \frac{dE(r)}{dr} + \frac{E(r)h^2(r)dh(r)}{4(1-\nu^2) dr} \right) \frac{d^2 \psi}{dr^2} + \left(\frac{\nu h^3(r)}{12r(1-\nu^2)} \frac{dE(r)}{dr} + \frac{E(r)h^3(r)}{12r^2(1-\nu^2)} + \frac{k_s^2 E(r)h(r)}{2(1+\nu)} + \frac{\nu E(r)}{4r(1-\nu^2)} \frac{dh(r)}{dr} \right) \frac{d\psi}{dr} - \left(\frac{k_s^2 E(r)h(r)}{2(1+\nu)} \right) \frac{dw}{dr}, \quad (\text{A.7})$$

$$K_{23} = \frac{\partial p^w}{\partial w} = - \left(\frac{k_s^2 E(r)h(r)}{2(1+\nu)} \right) \frac{d^2 w}{dr^2}, \quad (\text{A.8})$$

$$K_{31} = \frac{\partial p^w}{\partial u} = \left(\frac{\nu E(r)h(r)d^2 u}{(1-\nu^2)r dr^2} + \frac{E(r)h(r) du}{(1-\nu^2)r^2 dr} \right) \frac{dw}{dr} + \left(\frac{E(r)h(r)d^2 u}{(1-\nu^2) dr^2} + \frac{\nu E(r)h(r)du}{r(1-\nu^2) dr} \right) \frac{d^2 w}{dr^2}, \quad (\text{A.9})$$

$$K_{32} = \frac{\partial p^w}{\partial \psi} = \left(\frac{k_s^2 E(r)h(r)}{2(1+\nu)} \right) \frac{d^2 \psi}{dr^2} + \left(\frac{k_s^2 E(r)h(r)}{2r(1+\nu)} + \frac{k_s^2 h(r)}{2(1+\nu)} \frac{dE(r)}{dr} + \frac{k_s^2 E(r) dh(r)}{2(1+\nu) dr} \right) \frac{d\psi}{dr} + \left(\frac{k_s^2 E(r)h(r)}{2(1+\nu)} \right) \frac{d^2 w}{dr^2} + \left(\frac{k_s^2 E(r)h(r)}{2r(1+\nu)} + \frac{k_s^2 h(r)}{2(1+\nu)} \frac{dE(r)}{dr} + \frac{k_s^2 E(r) dh(r)}{2(1+\nu) dr} \right) \frac{dw}{dr} + \frac{\nu E(r)h(r)du}{(1-\nu^2)r dr} + \frac{E(r)h(r)}{(1-\nu^2)r^2} u + \frac{\nu E(r)h(r)}{2r(1-\nu^2)} \left(\frac{dw}{dr} \right)^2 \frac{dw}{dr} + \left(\frac{E(r)h(r)du}{(1-\nu^2) dr} + \frac{E(r)h(r)}{2(1-\nu^2)} \left(\frac{dw}{dr} \right)^2 + \frac{\nu E(r)h(r)}{r(1-\nu^2)} u \right) \frac{d^2 w}{dr^2}, \quad (\text{A.10})$$

$$K_{33} = \frac{\partial p^w}{\partial w} = \left(\frac{k_s^2 E(r)h(r)}{2(1+\nu)} \right) \frac{d^3 w}{dr^3} + \left(\frac{k_s^2 E(r)h(r)}{2r(1+\nu)} + \frac{k_s^2 h(r)}{2(1+\nu)} \frac{dE(r)}{dr} + \frac{k_s^2 E(r) dh(r)}{2(1+\nu) dr} + \frac{\nu E(r)h(r)du}{(1-\nu^2)r dr} + \frac{E(r)h(r)}{(1-\nu^2)r^2} u \right) \frac{d^2 w}{dr^2} + \left(\frac{\nu E(r)h(r)}{2r(1-\nu^2)} \right) \left(\frac{dw}{dr} \right)^2 \frac{d^2 w}{dr^2} + \frac{\nu E(r)h(r)}{r(1-\nu^2)} \left(\frac{dw}{dr} \right)^2 \frac{d^2 w}{dr^2} + \left(\frac{E(r)h(r)du}{(1-\nu^2) dr} + \frac{E(r)h(r)}{2(1-\nu^2)} \left(\frac{dw}{dr} \right)^2 + \frac{\nu E(r)h(r)}{r(1-\nu^2)} u \right) \frac{d^3 w}{dr^3}$$

$$+ \frac{E(r)h(r)}{(1-\nu^2)} \left(\frac{d^2 w}{dr^2} \right) \frac{dw}{dr}, \quad (\text{A.11})$$

References

- [1] M. Bayat, M. Saleem, B.B. Sahari, A.M.S. Hamouda, E. Mahdi, Analysis of functionally graded rotating disks with variable thickness, *Mechanics Research Communications* 35 (2008) 283–309.
- [2] H.M. Navazi, H. Haddadpour, Nonlinear cylindrical bending analysis of shear deformable functionally graded plates under different loadings using analytical methods, *International Journal of Mechanical Sciences* 50 (2008) 1650–1657.
- [3] M. Koizumi, The concept of FGM, *Ceramic Transactions on Functional Gradient Materials* 34 (1993) 3–10.
- [4] Y.A. Kang, X.F. Li, Bending of functionally graded cantilever beam with power-law non-linearity subjected to an end force, *International Journal of Non-Linear Mechanics* 44 (2009) 696–703.
- [5] A.M. Afsar, J. Go, Finite element analysis of thermoelastic field in a rotating FGM circular disk, *Applied Mathematical Modelling* 34 (2010) 3309–3320.
- [6] A. Nosier, F. Fallah, Non-linear analysis of functionally graded circular plates under asymmetric transverse loading, *International Journal of Non-Linear Mechanics* 44 (2009) 928–942.
- [7] J. Yang, H.S. Shen, Non-linear analysis of functionally graded plates under transverse and in-plane loads, *International Journal of Non-Linear Mechanics* 38 (2003) 467–482.
- [8] J.F. Durodola, O. Attia, Property gradation for modification of response of rotating MMC disks, *Journal of Materials Science and Technology* 16 (2000) 919–924.
- [9] S.A.H. Kordkheili, R. Naghdabadi, Thermoelastic analysis of a functionally graded rotating disk, *Composite Structures* 79 (2007) 508–516.
- [10] M. Asghari, E. Ghafoori, A three-dimensional elasticity solution for functionally graded rotating disks, *Composite Structures* 92 (2010) 1092–1099.
- [11] M. Bayat, M. Saleem, B.B. Sahari, A.M.S. Hamouda, E. Mahdi, Mechanical and thermal stresses in a functionally graded rotating disk with variable thickness due to radially symmetry loads, *International Journal of Pressure Vessels and Piping* 86 (2009) 357–372.
- [12] M. Bayat, M. Saleem, B.B. Sahari, A.M.S. Hamouda, E. Mahdi, On the stress analysis of functionally graded gear wheels with variable thickness, *International Journal for Computational Methods in Engineering Science and Mechanics* 9 (2008) 121–137.
- [13] E. Ghafoori, Comment on 'Thermoelastic analysis of the functionally graded rotating disk', *Composite Structures* 92 (2010) 2791–2792.
- [14] M. Bayat, B.B. Sahari, M. Saleem, A. Ali, S.V. Wong, Bending analysis of a functionally graded rotating disk based on the first order shear deformation theory, *Applied Mathematical Modelling* 33 (2009) 4215–4230.
- [15] M. Bayat, B.B. Sahari, M. Saleem, A. Ali, S.V. Wong, Thermoelastic solution of a functionally graded variable thickness rotating disk with bending based on the first-order shear deformation theory, *Thin-Walled Structures* 47 (2009) 568–582.
- [16] M. Bayat, M. Saleem, B.B. Sahari, A.M.S. Hamouda, E. Mahdi, Thermo elastic analysis of a functionally graded rotating disk with small and large deflections, *Thin-Walled Structures* 45 (2007) 677–691.
- [17] S. Sahraee, Bending analysis of functionally graded sectorial plates using Levinson plate theory, *Composite Structures* 88 (2009) 548–557.
- [18] E. Reissner, The effect of transverse shear deformation on the bending of elastic plates, *Journal of Applied Mechanics* 12 (1945) 69–77.
- [19] R.D. Mindlin, Influence of rotary inertia and shear on flexural motions of isotropic elastic plates, *Journal of Applied Mechanics* 18 (1951) 31–38.
- [20] A. Nosier, F. Fallah, Reformulation of Mindlin–Reissner governing equations of functionally graded circular plates, *Acta Mechanica* 198 (2008) 209–233.
- [21] A. Nosier, A. Yavari, S. Sarkani, Study of edge-zone equation of Mindlin–Reissner plate theory, *Journal of Engineering Mechanics* 126 (2000) 647–651.
- [22] A. Nosier, A. Yavari, S. Sarkani, On a boundary layer phenomenon in Mindlin–Reissner plate theory for laminated circular sector plates, *Acta Mechanica* 151 (2001) 149–161.
- [23] J.N. Reddy, C.M. Wang, S. Kitipornchai, Axisymmetric bending of functionally graded circular and annular plates, *European Journal of Mechanics: A/Solids* 18 (1999) 185–199.
- [24] J. Yang, H.-S. Shen, Nonlinear analysis of functionally graded plates under transverse and in-plane loads, *International Journal of Non-Linear Mechanics* 38 (2003) 467–482.
- [25] J.N. Reddy, C.L. Huang, Nonlinear axisymmetric bending of annular plates with varying thickness, *International Journal of Solids and Structures* 17 (1981) 811–825.
- [26] S.K. Jalali, M.H. Naei, A. Poorsolhjoui, Thermal stability analysis of circular functionally graded sandwich plates of variable thickness using pseudo-spectral method, *Materials & Design* 31 (2010) 4755–4763.
- [27] Y. Xu, D. Zhou, Three-dimensional elasticity solution of functionally graded rectangular plates with variable thickness, *Composite Structures* 91 (2009) 56–65.
- [28] T. Mori, K. Tanaka, Average stress in matrix and average elastic energy of materials with misfitting inclusions, *Acta Metallurgica* 21 (1973) 571–574.

- [29] B. Klusemann, B. Svendsen, Homogenization methods for multi-phase elastic composites: comparisons and benchmarks, *Technische Mechanik* 30 (4) (2010) 374–386.
- [30] A.J.M. Ferreira, R.C. Batra, C.M.C. Roque, L.F. Qian, P.A.L.S. Martins, Static analysis of functionally graded plates using third-order shear deformation theory and a meshless method, *Composite Structures* 69 (2005) 449–457.
- [31] X. Peng, X. Li, Thermal stress in rotating functionally graded hollow circular disks, *Composite Structures* 92 (2010) 1896–1904.
- [32] J.N. Reddy, *Theory and Analysis of Elastic Plates*, Taylor & Francis, Philadelphia, 1999.
- [33] A.N. Eraslan, H. Argeso, Limit angular velocities of variable thickness rotating disks, *International Journal of Solids and Structures* 39 (2002) 3109–3130.
- [34] A.S. Day, An introduction to dynamic relaxation, *The Engineer* 219 (1965) 218–221.
- [35] M. Salehi, A.R. Sobhani, Elastic linear and non-linear analysis of fiber-reinforced symmetrically laminated sector Mindlin plate, *Composite Structures* 65 (2004) 65–79.
- [36] G.J. Turvey, M. Salehi, Elasto-plastic large deflection response of pressure loaded circular plates stiffened by a single diametral stiffener, *Thin-Walled Structures* 46 (2008) 991–1002.
- [37] M. Kadkhodayan, L.C. Zhang, R. Sowerby, Analysis of wrinkling and buckling of elastic plates by DXDR method, *Computers and Structures* 65 (1997) 561–574.
- [38] M.E. Golmakani, M. Kadkhodayan, Nonlinear bending analysis of annular FGM plates using higher-order shear deformation plate theories, *Composite Structures* 93 (2011) 973–982.
- [39] L.C. Zhang, T.X. Yu, Modified adaptive dynamic relaxation method and its application to elastic-plastic bending and wrinkling of circular plates, *Computers and Structures* 33 (1989) 609–614.
- [40] L.C. Zhang, M. Kadkhodayan, Y.W. Mai, Development of the maDR method, *Computers and Structures* 52 (1994) 1–8.
- [41] P. Underwood, *Dynamic relaxation*, *Computational Methods for Transient Analysis*, Elsevier, Amsterdam (1983) 245–256. (Chapter 5).
- [42] M. Papadrakakis, A method for the automatic evaluation of the dynamic relaxation parameters, *Computer Methods in Applied Mechanics and Engineering* 25 (1981) 35–48.
- [43] S.P. Timoshenko, *History of Strength of Materials*, McGraw-Hill, New York, 1953.
- [44] H. Kobayashi, G.J. Turvey, On the application of a limiting process to the dynamic relaxation analysis of circular membranes, circular plates and spherical shells, *Computers and Structures* 48 (6) (1993) 1107–1116.
- [45] L.S. Ma, T.J. Wang, Nonlinear bending and post-buckling of a functionally graded circular plate under mechanical and thermal loadings, *International Journal of Solids and Structures* 40 (2003) 3311–3330.
- [46] G.J. Turvey, N.G.V. Der Avanessian, Elastic large deflection analysis of ring-stiffened circular plates using graded finite-differences, in: *Proceedings of the First International Conference on Numerical Methods in Engineering: Theory and Applications*, Swansea, 1985, pp. 875–884.